SECTION 1

RESEARCH IN PROGRESS

NUCLEAR REACTIONS -- EXPERIMENTAL

FRAGMENTATION OF ^{86}Kr AT 70 MeV/NUCLEON

R. Pfaff, M. Fauerbach, M. Hellström, J. H. Kelley, R.A. Kryger, D.J. Morrissey, B.M. Sherrill, M. Steiner, J.S. Winfield, J.A. Winger, and B.M. Young.

Projectile fragmentation has proven to be an effective method to produce many exotic nuclei. The production of beam velocity residues from the projectile is relatively well understood in both the high energy (E > 200 MeV/nucleon) and low energy (E < 20 MeV/nucleon) domains. At relativistic energies 'pure' fragmentation occurs while the low energy domain is dominated by deep-inelastic scattering processes. The interpretation of the intermediate energy domain (20 MeV/nucleon < E < 200 MeV/nucleon) is not so well understood due to the limited availability of data, particularly for reactions involving medium-mass and heavy nuclei.

It is crucial for the planning of future experiments with secondary beams that the production yields of exotic nuclei produced in intermediate energy reactions can be accurately predicted. To make these predictions, we need a better understanding of the interplay between competing reaction mechanisms present in this energy region, and to map out the gradual transition from the deep inelastic processes of the low-energy regime to the more violent collisions at relativistic energies. The aim of this study – together with other experiments performed at the National Superconducting Cyclotron Laboratory (NSCL) and elsewhere – is to close the gap in our knowledge by providing high-quality data on production yields and momentum distributions for the "fragmentation" of heavy projectiles with a broad range of energies[1,2,3].

This report presents the analysis of an experiment performed at the NSCL using the A1200 mass separator[4]. The techniques used to identify fragments have been described in detail elsewhere[5]. The experiment used a 0.6 pnA 70 MeV/nucleon ^{86}Kr beam from the K1200 cyclotron, incident on a 4 mg/cm^2 Al target placed at the medium acceptance target position of the A1200. We obtained ΔE, E, time-of-flight, and rigidity information from which the mass A, proton number Z, and charge state Q of the individual isotopes were determined using well known formulae[6]. The measurements had resolutions (FWHM) of Δ A/A = 0.3, ΔZ/Z = 0.4, and ΔQ/Q = 0.3, allowing clear separation of the fragments. Momentum distributions were obtained for sixty-three individual isotopes. The parallel momentum distribution of each isotope was fitted to a Gaussian function, from which the parallel momentum width, the momentum transfer, and the isotope yield was determined. Data for the projectile-like fragments ranging from Z=33 to Z=39 are presented below.

The measured values of the parallel momentum widths and the predictions of the Goldhaber model[7] are shown in Figure 1, along with the predictions from the high-energy systematics previously obtained by Morrissey[8]. The Goldhaber model was developed for data from high energy fragmentation and is based on the fact that removing independent nucleons from the projectile results in a Gaussian momentum distribution. The parallel momentum width predicted by the Goldhaber model is directly proportional to the Fermi momentum of individual nucleons in the participants and is shown by the solid curve in Figure 1 (corresponding to p_F = 275 MeV/c). The value is somewhat higher than a value obtained using quasi-elastic electron scattering data[9] where p_F = 260 MeV/c and also higher than the values of p_F that typically have been used to fit high energy fragmentation data. This noticeable increase in the parallel momentum width could be caused by other reaction processes that will occur in the intermediate energy regions but would not be present in the high energy domain where 'pure' fragmentation occurs. The dashed curve shown in Figure 1 is calculated from the systematics of Morrissey[8] that was obtained from parameterization of high energy fragmentation data. The latter prediction also agrees fairly well with the data as did the fit from the Goldhaber model.

Widths of Parallel Momentum Distributions
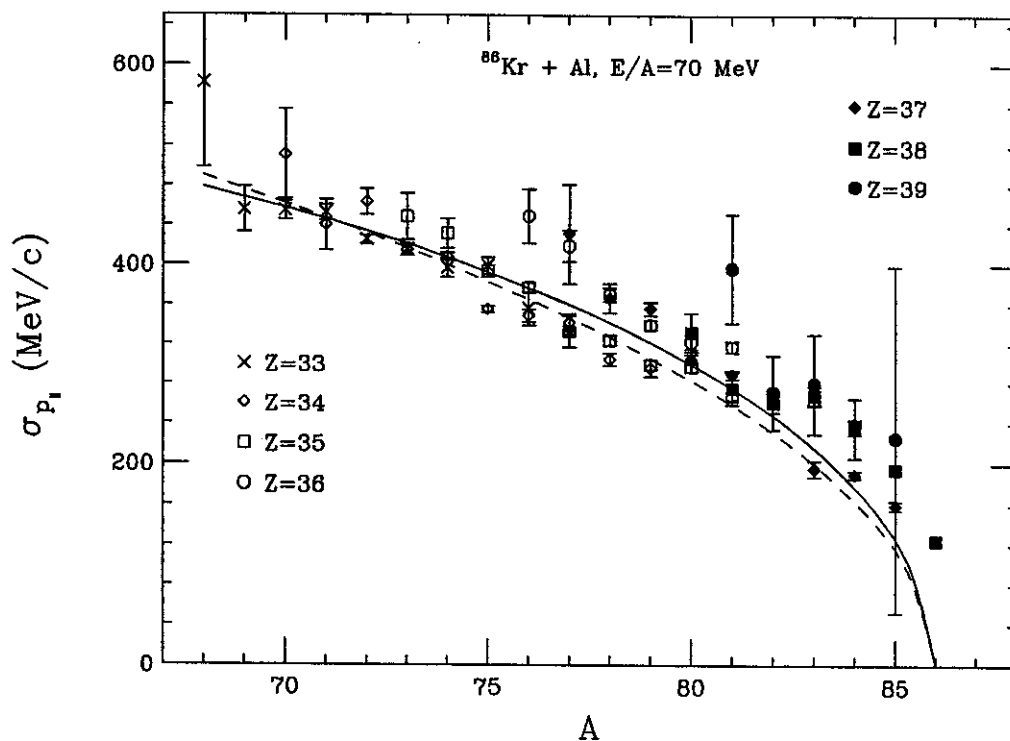
^{86}Kr + Al, E/A=70 MeV

Figure 1: Widths of parallel momentum distributions compared to predictions using the Goldhaber model (solid line)[7] and the systematics of Morrissey (dashed line)[8]. The solid symbols indicate charge pick-up products. The error bars are indicative of the statistical error only and do not include any uncertainties due to beam normalization.

The average parallel momentum transfer $\langle P'_{\parallel} \rangle$ is shown in Figure 2, note that the charge pick-up products are indicated by solid symbols. Morrissey[8] has defined this quantity as the product of the projectile mass, the average velocity of the fragment $\langle \beta_{\parallel} \rangle$, and a kinematic factor of $\beta \gamma/(\gamma+1)$ and has shown that a linear relationship exists between $\langle P'_{\parallel} \rangle$ and the product of the number of nucleons removed from the projectile ΔA, and a slope parameter of -8 MeV/c. This dependence was also derived from high energy fragmentation data. The solid line shown in Figure 2 is the result of a linear fit to the fragment data with $Z \leq 36$. The present slope parameter of -8.8 MeV/c is in good agreement with the overall trend of the 'pure' fragmentation products. When individual elements are considered, the best-fit slope parameters are greater than the overall slope, as is shown in Figure 3. Large slope parameters (-14 MeV/c through -58 MeV/c) have recently been reported for projectile-like fragments from the high energy fragmentation of ^{86}Kr[2], as well as other high energy data[10]. The slope parameters of the present data do not show the significant changes seen in the high energy data. It has been suggested[2] that this could be caused by the fact that the very neutron-rich fragments are more sensitive to the first collisional step of fragmentation than to the second evaporative step whereas the opposite is true of the proton-rich fragments. In the intermediate energy regime it is possible that the initial violence of the collisions is reduced and the pre-fragment is not as excited, thus producing less dramatic changes in the slope parameter than is observed in fragmentation at high energy.

More interesting, the parallel momentum transfer of the charge pick-up products systematically deviates from the high energy systematics as the number of protons gained in the reaction increases. A simple momentum conservation model[1] that relies on the pick-up of protons (nearly at rest) from the target nucleus partially explains the data. The model assumes that the projectile interacts with the target nucleons

2

and, on average, picks up protons that are moving parallel to the projectile at the Fermi momentum. The model shows that the momentum of the pick-up product is given by

$$\frac{\langle p_F \rangle}{A_F} = \frac{p_P}{A_P} - \frac{\Delta A_t}{A_F}\left(\frac{p_P}{A_P} - p_{Fermi}\right)$$

where ΔA_t is the number of picked-up nucleons, p_F is the fragment momentum, p_P is the projectile momentum, A_P is the projectile mass, A_F is the fragment mass, and p_{Fermi} is the Fermi momentum. The dashed lines in Figure 2 show the predictions of this model with a value of 200 MeV/c used for the Fermi momentum. The agreement with the rubidium (Z=37) data is not good, indicating that these isotopes follow the 'pure' fragmentation process with little preferential proton pick-up. However, the yttrium isotopes (Z=39) do follow the prediction relatively well, indicating that preferential proton pick-up is the primary reaction process for these nuclei.
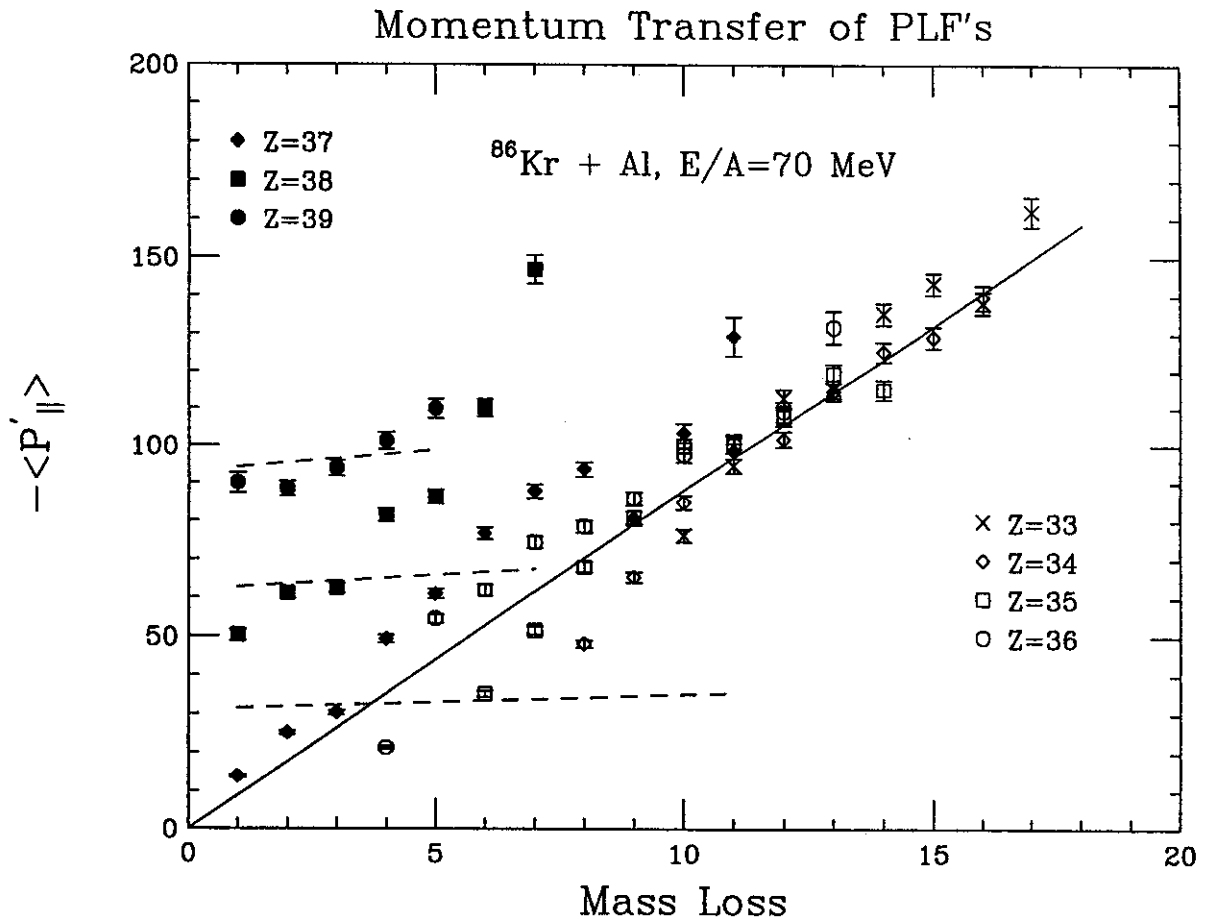

Figure 2: Momentum transfer vs. mass loss (A_{proj}-A_{frag}). The solid line indicates the linear relationship between momentum transfer and mass loss shown by Morrissey[8]. A slope parameter of -8.8 MeV/c is the best linear fit to the fragmentation products (Z ≤ 36). The predictions for the proton pick-up products (Z ≥ 37) are shown with dashed lines and are calculated from a momentum conservation model[1] in which protons are preferentially picked-up from the target with a momentum oriented along the direction of the projectile motion (a value of p_{Fermi} = 200 MeV/c was used for this calculation).
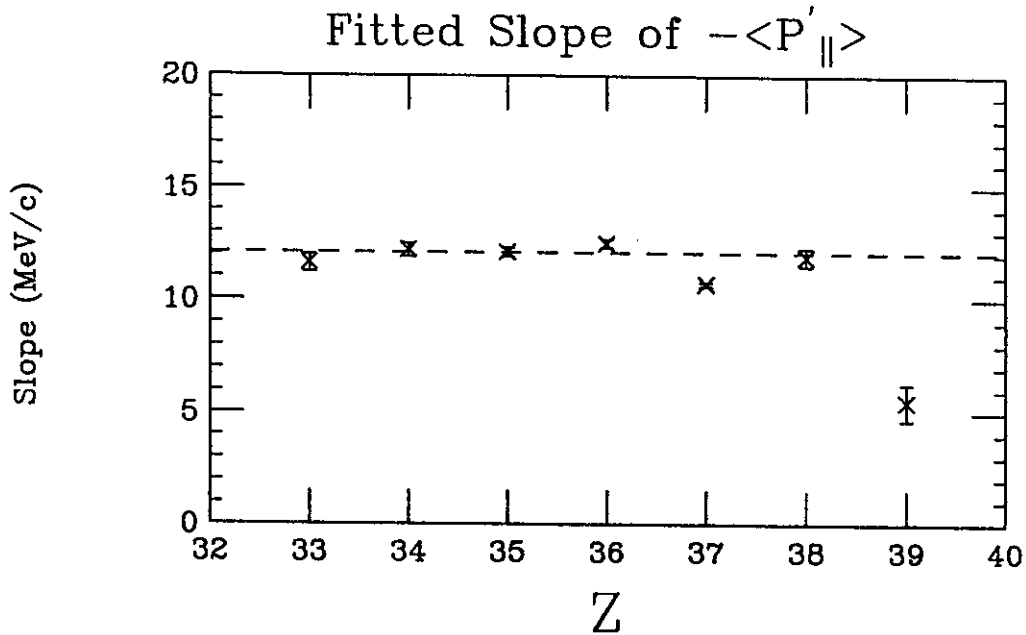
3

Figure 3: The slope parameters for the individual elements. The dashed line is the best fit line of the fragmentation isotopes (Z≤36) and has a value of 12.2 MeV/c which is greater than the overall trend of the data shown in Figure 2. The error bars are statistical.

Shown in Figure 4 are the relative total yields for the Z=33 (arsenic) through Z=39 (yttrium) isotopes that were obtained by integrating the Gaussian fits of the parallel momentum distributions over momentum space. The error bars shown are indicative of the statistical error only and do not include any uncertainties due to the beam normalization. The histograms represent calculations from the internuclear cascade model ISApace[11]. This model is considered valid between a few hundred MeV/nucleon and one GeV/nucleon and uses the Yariv-Fraenkel ISABEL internuclear code[12] followed with the PACE evaporative code[13]. All the yields produced by the ISApace code were scaled with a single normalization obtained by matching the actual yield of ^{82}Kr to the calculated yield. The relative yield and shape of the predicted yields are in remarkable agreement with the fragmentation products (Z≤36), however the yields of the charge pick-up products are significantly greater than the ISApace predictions. This difference grows as the number of protons acquired increases (although the shape is reproduced rather well). These comparisons indicate that even at the transitional energy of 70 MeV/nucleon, 'pure' fragmentation is important while at the same time other processes are occurring – most notably in the charge pick-up products, where the high-energy models are not able to reproduce the experimental data.

The dotted histograms shown in Figure 4 are the predictions of the INTENSITY code[14] which uses the high energy systematics established by Sümmerer et al.[15]. The calculations of INTENSITY were also scaled with a normalization factor to reproduce the actual ^{82}Kr yield. The relative yields predicted by the code are generally higher than the observed yields for the neutron-rich isotopes while underpredicting the proton-rich isotopes. This indicates that the evaporative step of fragmentation contributes significantly to the proton-rich side of the isotopic chains. The relative yields of the charge pick-up products are also tremendously underpredicted as is expected for high energy reactions.
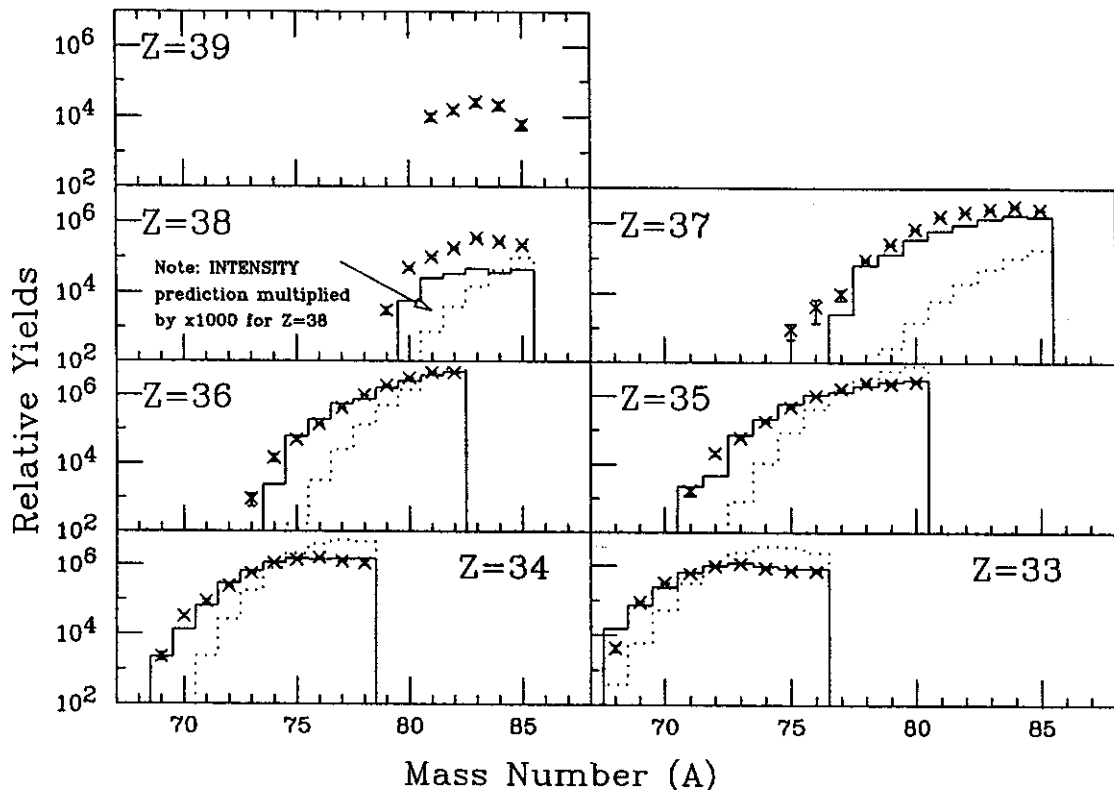
4

Figure 4: The relative isotopic yields for the elements between arsenic (Z=33) and yttrium (Z=39). The solid histograms are predictions from the internuclear-cascade model ISApace[11] and the dotted histograms are predictions from the INTENSITY code[14] that is based on the EPAX parameterization[15].

References

1. G.A. Souliotis et al., Phys. Rev. C46 (1992) 1383.
2. M. Weber et al., GSI-94-29 Preprint, April 1994, submitted to Nucl. Phys. A.
3. C. Stèphan et al., Phys. Lett. B262 (1991) 6.
4. B.M. Sherrill et al., Nucl. Instrum. Methods B56 (1991) 1106.
5. R. Pfaff et al., MSU/NSCL Annual Report (1992) 61.
6. D. Bazin et al., Nucl. Phys. A515 (1990) 349.
7. A.S. Goldhaber, Phys. Lett. B53 (1974) 306.
8. D.J. Morrissey, Phys. Rev. C39 (1989) 460.
9. E.J. Moniz et al., Phys. Rev. Lett. 26 (1971) 445.
10. J. Friese et al., Proc. of the 3rd Int. Conf. on Radioactive Nuclear Beams (East Lansing, USA, May 1993) D.J. Morrissey, Ed., Edition Frontiers (Gif-sur-Yvette, France, 1993) 333.
11. M. Fauerbach, Diploma thesis, TH Darmstadt, (1992).
12. Y. Yariv and Z. Fraenkel, Phys. Rev. C20 (1979) 2227.
13. A. Gavron, Phys. Rev. C12 (1980) 230.
14. J.A. Winger, B.M. Sherrill, and D.J. Morrissey, Nucl. Instrum. Methods B70 (1992) 380.
15. K. Sümmerer et al., Phys. Rev. C42 (1990) 2546.

OBSERVATION OF LIFETIME EFFECTS IN TWO-PROTON CORRELATIONS FOR WELL-CHARACTERIZED SOURCES

M.A. Lisa[a], C.K. Gelbke, P. Decowski[b], W.G. Gong[a], E. Gualtieri, S. Hannuschke, R. Lacey[c], T. Li, W.G. Lynch, G.F. Peaslee[d], S. Pratt, T. Reposeur[e], A.M. Vander Molen, G.D. Westfall, J.Yee, and S.J. Yennello[f]

Two-proton correlation functions at small relative momenta probe the space-time geometry of the emitting system, because the magnitude of nuclear and Coulomb final-state interaction and antisymmetrization effects depends on the spatial separation of the emitted particles [1-29]. The attractive S-wave nuclear interaction leads to a pronounced maximum in the correlation function at relative momentum $q \approx 20$ MeV/c. This maximum decreases for increasing source dimensions and/or emission time-scales. The Coulomb interaction and antisymmetrization produce a minimum at $q \approx 0$. Non-spherical phase-space distributions, predicted for long-lived emission sources, can lead to a dependence of the two-proton correlation function on the direction of the relative momentum [13,23]. Until now, however, such directional dependences have not yet been observed unambiguously [16,18,21,24,25,29], possibly because a clear characterization of emission sources was not achieved in previous experiments [29,30].
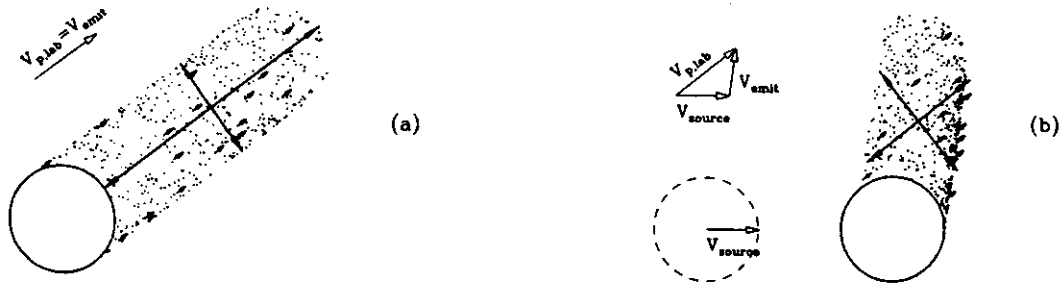

Figure 1: Schematic illustration of phase space distributions at a time $t = 70$ fm/c, seen by a detector at $q_{lab} = 38°$, for a spherical source of radius $r = 3.5$ fm and lifetime $t = 70$ fm/c emitting protons of momentum 250 MeV/c. Details are discussed in the text.

The problem of identifying finite-lifetime effects is illustrated in Fig. 1. The figure depicts phase space distributions in the laboratory rest frame of protons emitted with fixed laboratory velocity $v_{p, lab}$ towards the detector at $q_{lab} = 38°$ for a source at rest in the laboratory (part a) and for a source at rest in the center-of-momentum system of projectile and target ($v_{source} = 0.18c$, part b). We assumed a spherical source of 7 fm diameter and 70 fm/c lifetime emitting protons of momentum 250 MeV/c.
For emission from a source at rest, the phase space distribution of particles moving with a fixed velocity $v_{p,lab} = v_{emit}$ towards the detector exhibits an elongated shape [13,24,32] oriented parallel to $v_{p,lab}$. A source of lifetime t appears elongated in the direction of the proton momentum by an incremental distance $Ds \approx v_{emit} \cdot t = v_{p,lab} \cdot t$. Correlation functions for relative momenta $q \wedge v_{p,lab}$ reflect a stronger Pauli-

suppression, and hence a reduced maximum at $q \approx 20$ MeV/c, than those for $q \parallel v_{p,lab}$ [13,23,24,32].

Cuts on the relative orientation of q and P are sensitive to the motion of the source, since the direction of the total momentum depends on rest frame, while the direction of the relative momentum— at least in the nonrelativistic limit— does not. Previous analyses [2,16,21,24,25] compared the shapes of correlation functions selected by cuts on the relative angle $y_{lab} = \cos^{-1}(q \cdot P/qP)$ between q and $P = p_1 + p_2 \approx 2mv_{p,lab}$, where p_1 and p_2 are the laboratory momenta of the two protons and q is the momentum of relative motion. Such analyses are optimized to detect lifetime effects of sources stationary in the laboratory system, but they can fail to detect lifetime effects for non stationary sources. For the specific case illustrated in Fig. 1b, the source dimensions parallel and perpendicular to $v_{p,lab}$ are very similar, and no significant differences are expected for the corresponding longitudinal and transverse correlation functions.

For a source of known velocity, the predicted lifetime effect is detected most clearly if longitudinal and transverse correlation functions are selected by cuts on the angle $y_{source} = \cos^{-1}(q' \cdot P'/q'P')$, where the primed quantities are defined in the rest frame of the source. (In the frame of the source, the phase space distribution is always elongated in the direction of v_{emit}. Hence, in Fig. 1b, the source dimensions should be compared in directions parallel and perpendicular to v_{emit}.) Such analyses can only be carried out for emission from well characterized sources [29].
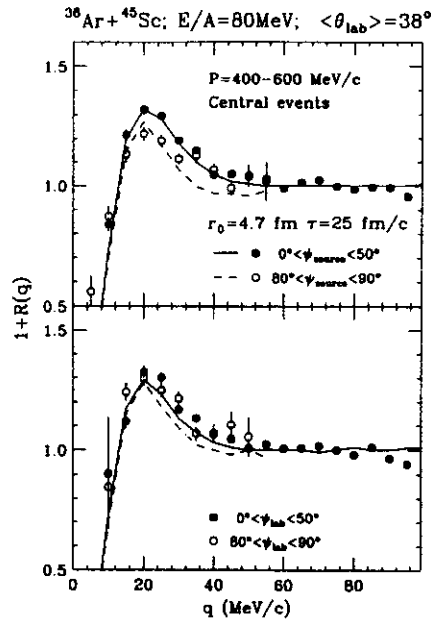

Figure 2: Measured longitudinal and transverse correlation functions for protons emitted in central [36]Ar + [45]Sc collisions at E/A = 80 MeV. Details are discussed in the text.

Figure 2 shows longitudinal and transverse two-proton correlation functions for central [36]Ar + [45]Sc collisions at E/A = 80 MeV constructed by the singles technique [31] selected by appropriate cuts [32] on the total transverse energy detected in the 4p Array. In a geometrical picture [33,34], the applied cuts correspond to reduced impact parameters [34] of $b/b_{max} = 0 - 0.36$. Longitudinal (solid points) and transverse (open points) correlation functions were defined by cuts on the angle $y = \cos^{-1}(q \cdot P/qP) = 0°-50°$ and $80°-90°$, respectively. (The normalization constant C in Eq. 1 is independent of y.) To maximize lifetime effects and reduce contributions from the very early stages of the reaction, the coincident proton pairs were selected by a low-momentum cut [33] on the total laboratory momentum, $P = 400-600$ MeV/c.

The top panel shows correlation functions for which the angle y was defined in the center-of-momentum frame of projectile and target (y = y_{source}); for central collisions of two nuclei of comparable mass, this rest frame should be close to the rest frame of the emitting source. The bottom panel shows correlation functions for which the angle y was defined in the laboratory frame (y = y_{lab}).

Consistent with the qualitative arguments presented in Fig. 1, a clear difference between longitudinal and transverse correlation functions is observed for cuts on y_{source} (top panel of Fig. 2), but not for cuts on y_{lab} (bottom panel of Fig. 2). The suppression of the transverse correlation function with respect to the longitudinal correlation function observed in the top panel in Fig. 2 is consistent with expectations for emission from a source of finite lifetime [13,23,24,32]. The solid and dashed curves in the top and bottom panels of Fig. 2 depict calculations for emission from a spherical Gaussian source co-moving with the center-of-momentum frame of the projectile and target. The calculations were performed for the radius and lifetime parameters r_0 = 4.7 fm and t = 25 fm/c, see also Eq. 2 below.

For a more quantitative analysis, we performed calculations assuming a simple family of sources of lifetime t and spherically symmetric Gaussian density profiles, moving with the center-of-momentum frame of reference. Energy and angular distributions of the emitted protons were selected by randomly sampling the experimental yield Y(p). Specifically, the single particle emission functions [23,24] were parametrized as

$$g(\mathbf{r},\mathbf{p},t) \propto \exp(-r^2/r_o^2 - t/\tau) \cdot Y(\mathbf{p}). \tag{2}$$

In Eq. 2, $\mathbf{r}$, $\mathbf{p}$, and t refer to the rest frame of the source. Phase-space points generated in the rest frame of the source were Lorentz boosted into the laboratory frame, and the two-proton correlation function was obtained by convolution with the two-proton relative wavefunction, see refs. [13,23,24] for details.

Transverse and longitudinal correlation functions were calculated for the range of parameters r_0 = 2.5 - 6.0 fm and t = 0 - 150 fm/c. For each set of parameters, the agreement between calculated and measured longitudinal and transverse correlation functions was evaluated by determining the value of c^2/n (chi-squared per degree of freedom) in the peak region, q = 15 - 30 MeV/c. Good agreement between calculations and data is obtained for source parameter values of roughly r_0=4.5-4.8 fm and t = 20-40 fm/c. (Comparison of the data to correlations predicted for surface emission from a spherical sphere leads to source parameters of R=6.5-8.0 fm and t = 30-50 fm/c.) These extracted emission timescales are qualitatively consistent with those predicted by microscopic transport calculations [22-24].

a. Present address: Lawrence Berkeley Laboratory, Berkeley, CA 94720
b. Present address: Department of Physics, Smith College, Northampton, MA
c. Present address: Department of Chemistry, State University of New York, Stony Brook, NY 11776
d. Present address: Department of Chemistry, Hope College, Holland, MI
e. Present address: Laboratoire de Physique Nucléaire, Université de Nantes, Nantes Cedex 03, France
f. Present address: Cyclotron Instiitute, Texas A&M University, College Station, TX 77843

References

1.   S.E. Koonin, Phys. Lett. **B70**, 43 (1977).
2.   F. Zarbaksh et al., Phys. Rev. Lett. **46**,1268 (1981).
3.   W.G. Lynch et al., Phys. Rev. Lett. **51**, 1850 (1983).
4.   W.G. Lynch et al., Phys. Rev. Lett. **52**, 2302 (1984).
5.   H. A. Gustafsson et al., Phys. Rev. Lett. **53**, 544 (1984).
6.   C.B. Chitwood et al., Phys. Rev. Lett. **54**, 302 (1985).
7.   J. Pochodzalla et al., Phys. Lett. **B174**, 36 (1986).
8.   A. Kyanowski et al., Phys. Lett. **B181**, 43 (1986).
9.   J. Pochodzalla et al., Phys. Rev. **C35**, 1695 (1987).
10.   Z. Chen et al., Phys. Rev. **C36**, 2297 (1987).

11. Z. Chen et al., Phys. Lett. **B186**, 280 (1987).
12. Z. Chen et al., Nucl. Phys. **A473**, 564 (1987).
13. S. Pratt and M.B. Tsang, Phys. Rev. **C36**, 2390 (1987).
14. P. Depieux et al., Phys. Lett. **B200**, 17 (1988).
15. D. Fox et al., Phys. Rev. **C38**, 146 (1988).
16. T.C. Awes et al., Phys. Rev. Lett. **61**, 2665 (1988).
17. P.A. DeYoung et al., Phys. Rev. **C39**, 128 (1989).
18. D. Ardouin et al., Nucl. Phys. **A495**, 57c (1989).
19. P.A. DeYoung et al., Phys. Rev. **C41**, R1885 (1990).
20. D.H. Boal et al., Rev. Mod. Phys. **62**, 553 (1990).
21. W.G. Gong et al., Phys. Lett. **B246**, 21 (1990).
22. W.G. Gong et al., Phys. Rev. Lett. **65**, 2114 (1990).
23. W.G. Gong et al. Phys. Rev. **C43**, 781 (1991).
24. W.G. Gong et al., Phys. Rev. **C43**, 1804 (1991).
25. D. Goujdami et al., Z. Phys. **A339**, 293 (1991).
26. B. Erazmus et al. Phys. Rev. **C44**, 2663 (1991).
27. M. Korolija et al., Phys. Rev. Lett. **67**, 572 (1991)
28. W. Bauer et al., Annu. Rev. Nucl. Part. Sci. **42**, 77 (1992).
29. D. Rebreyend et al., Phys. Rev. **C46**, 2387 (1992).
30. A weak signal of marginal statistical significance was reported in ref. [25].
31. G.F. Bertsch, Nucl. Phys. **A498**, 173c (1989).
32. M.A. Lisa, et. al. Phys. Rev. Lett. **71**, 2863 (1993)
33. M.A. Lisa, Ph.D. Thesis, Michigan State University, (1993)
34. L. Phair et al., Nucl. Phys. **A548**, 489 (1992)

SOURCES AND EMISSION TIME SCALES IN E/A = 50 MeV
^{129}Xe + ^{nat}Cu REACTIONS

D.R. Bowman[a], G.F. Peaslee[b], N. Carlin[c], R.T. de Souza[d], C.K. Gelbke, W.G. Gong[e], Y.D. Kim[f], M.A. Lisa[e], W.G. Lynch, L. Phair[e], M.B. Tsang, C. Williams, N. Colonna[i], K. Hanold[e], M.A. McMahan[e], G.J. Wozniak[e], and L.G. Moretto[e]

Studies of fragment-fragment correlations have indicated fragment emission time scales ≤ 100-200 fm/c, consistent with fast, nonsequential breakup processes [1, 2]. In these measurements, central collisions were selected by multiplicity cuts, but no detailed information about the sources of the fragments was obtained. In this work we characterize the sources of fragment emission in both central and peripheral collisions by measuring fragment velocity distributions, and experimentally determine the time scales associated with fragment emission from these sources.

The experiment was performed using the K1200 Cyclotron at the National Superconducting Cyclotron Laboratory at Michigan State University. A beam of ^{129}Xe ions with intensity $\sim 10^7$ particles/s impinged upon ^{nat}Cu targets of thickness 2 mg/cm^2. Intermediate mass fragments and light charged particles were detected at angles of 16°-160° using the MSU Miniball phoswich array [3], which covered approximately 87% of 4π. At more forward angles, 2°-16°, 16 position-sensitive Si-Si(Li)-Plastic telescopes were placed [4]. The energy calibrations are estimated to be accurate to 1% for fragments stopped in the Si(Li) detectors and 5-10% for fragments and particles detected with the Miniball. The position resolution of the Si telescopes is approximately ±1.5 mm in both the X and Y dimensions.

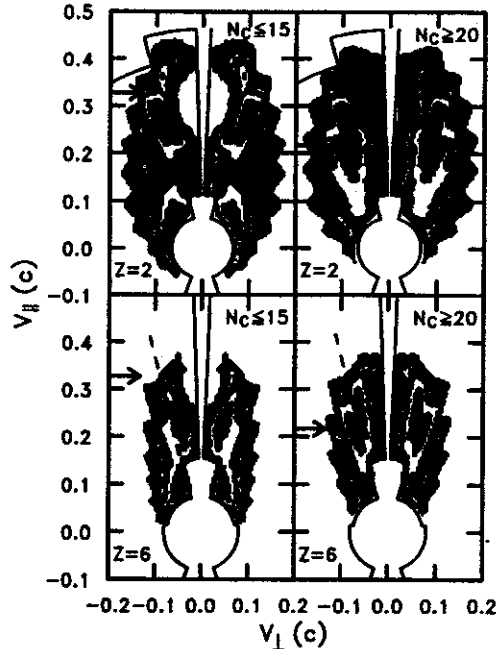Figure 1 shows the cross sections in velocity space for Z=2 and Z=6 fragments with two different

Figure 1: Density plots of $d^2\sigma/dv_\parallel dv_\perp$ for Z=2 (top panels) and Z=6 (bottom panels) fragments. Distributions gated on low (high) charged particle multiplicity, N_C, are shown in the left (right) panels. The limits of the (Si) detector acceptance are indicated by the solid (dashed) lines. The arrows in the left (right) panels indicate the beam (center-of-mass) velocity.

gates on the total charged particle multiplicity, N_C. The limits of detector acceptance are indicated by the solid lines. Peripheral collisions (left hand panels) show one component centered at a parallel velocity slightly less than that of the beam (arrows) and a second component centered at a parallel velocity slightly larger than zero. We interpret these components as due to the decay of projectile-like (PLF) and target-like fragments (TLF). These fragments are not completely equilibrated since the emission is preferentially backward in the frame of the PLF, and preferentially forward in the frame of the TLF, which leads to enhanced fragment yields at intermediate velocities. This enhancement is particularly evident for the Z=6 fragments. Fits of such velocity distributions require emission from three (isotropic) sources: a PLF, a TLF, and a third "nonequilibrium" source with a velocity approximately one-half of that of the beam (nucleon-nucleon center-of-mass frame) [1, 5].

The right hand panels in Figure 1 show velocity distributions for Z=2 and Z=6 fragments gated on high multiplicity collisions. These distributions are broad, anisotropic, and centered at approximately the projectile-target center-of-mass velocity (arrows on right hand panels).

In order to obtain quantitative information about the time scales of fragment emission we have constructed two-fragment, velocity correlation functions defined as:

$$\sum Y_{12}(\mathbf{v_1}, \mathbf{v_2}) = C[1 + R(v_{red})] \sum Y_1(\mathbf{v_1}) Y_2(\mathbf{v_2}),$$

where $\mathbf{v_1}$ and $\mathbf{v_2}$ are the laboratory velocities of the fragments, v_{red} is the reduced relative velocity, $v_{red} = (\mathbf{v_1} - \mathbf{v_2})/\sqrt{Z_1 + Z_2}$, and C is a normalization constant determined by requiring $R(v_{red}) \approx 0$ at large relative velocities where the final state interaction is small. The singles yields, Y_1 and Y_2, are taken from the same events as the coincidence yield, Y_{12}. The reduced relative velocity, v_{red}, is introduced to eliminate the charge dependence of the relative fragment velocity in mixed fragment correlation functions [1]. We have verified with $Z_1 = Z_2$ correlation functions that there is little dependence of v_{red} on Z for $v_{red} > 0.01c$.

In Figure 2, we show mixed fragment correlation functions ($5 \leq Z_1, Z_2 \leq 12$) for fragments stopped in the Si(Li) detectors. The limits of acceptance of these detectors, $2° < \theta_1, \theta_2 < 16°$, are shown by the dashed lines in the bottom panels of Fig. 1. The top and bottom panels of this Fig. 2 show correlation functions gated on high and low multiplicity collisions, respectively. To enhance contributions from the projectile-like source, the low multiplicity correlation functions are also gated on a center-of-mass (CM) velocity of the two fragments of $V_{CM} > 0.3c$. The two correlation functions exhibit dramatic differences in shape. For $V_{CM} > 0.3c$ there is a maximum at $v_{red} = 0.017c$.

Let us first consider the peripheral reactions [6]. Simulated events from a three-body trajectory calculation [1] were generated using the experimental charge, energy, and angular distributions; subsequently filtered through a software replica of the experimental apparatus; and analyzed in the same manner as the experimental data. The calculated correlation functions are sensitive to the space-time extent of the emitting source. In the simulations we have fixed the source radius, R_S, at 10 fm and the total charge, mass, and velocity of the system at 54, 129, and 0.33c, respectively, equal to the projectile charge, mass and velocity. In the bottom panel of Fig. 2, the simulated correlation function with mean emission times, τ, of 100, 200, and 500 fm/c are compared with the experimental data; a mean emission time of 200 fm/c gives the best agreement [7]. We have performed other calculations with identical emission times and $R_S = 8$ and 12 fm [8]. To quantify the agreement between the simulations and the experimental data, the reduced χ^2 values are presented in Table 1 [9]. For any reasonable choice of radius parameter, the time scale for emission of high velocity fragments in peripheral reactions is on the order of 200-500 fm/c.

Now let us consider the central reactions. We have not placed a gate on CM velocity due to the
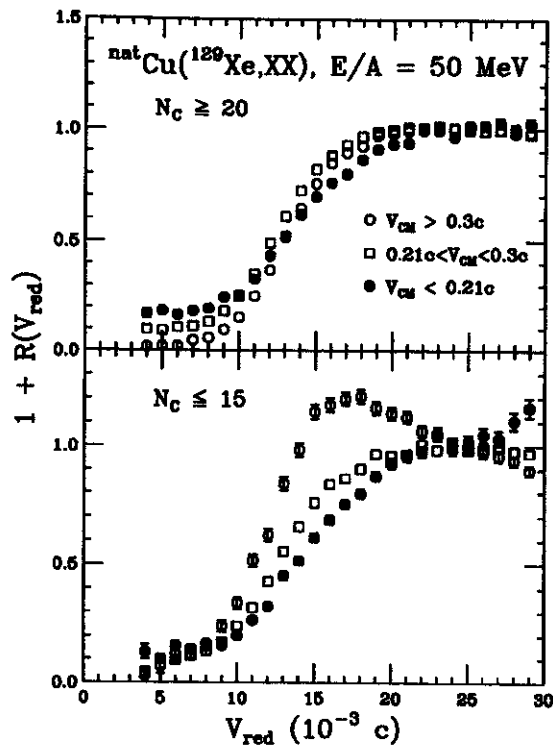
11

Figure 2: Experimental correlation functions for $5 \leq Z_1, Z_2 \leq 12$ fragments as a function of the reduced relative velocity, v_{red}. The top (bottom) panel corresponds to high (low) multiplicity events. The solid circles, open circles, and open squares correspond to events gated on the indicated ranges of center-of-mass velocity of the two fragments.

single apparent source observed in the velocity distributions (Fig. 1). For these simulations we have chosen a source charge, mass, and velocity of 83, 193, and 0.22 c, respectively, corresponding to complete fusion of projectile and target. In the top panel of Fig. 3 the experimental data for high multiplicity

Table 1: Reduced chi-squared values, χ^2/ν, for calculated correlation functions for fragment pairs with $V_{CM} > 0.3c$ in low multiplicity collisions.

τ (fm/c)	R_S (fm)		
	8	10	12
500	8.3	14.5	19.4
200	8.8	8.2	4.8
100	76.7	49.5	24.8

Table 2: Reduced chi-squared values, χ^2/ν, for calculated correlation functions in high multiplicity collisions.

τ (fm/c)	R_S (fm)		
	10	12	14
200	54.3	83.7	106.1
100	7.0	3.5	23.1
50	177.4	32.3	3.8
0	704.5	147.5	26.6

collisions are compared with three-body trajectory calculations with R_S=12 fm and τ=0, 50, 100, and 200
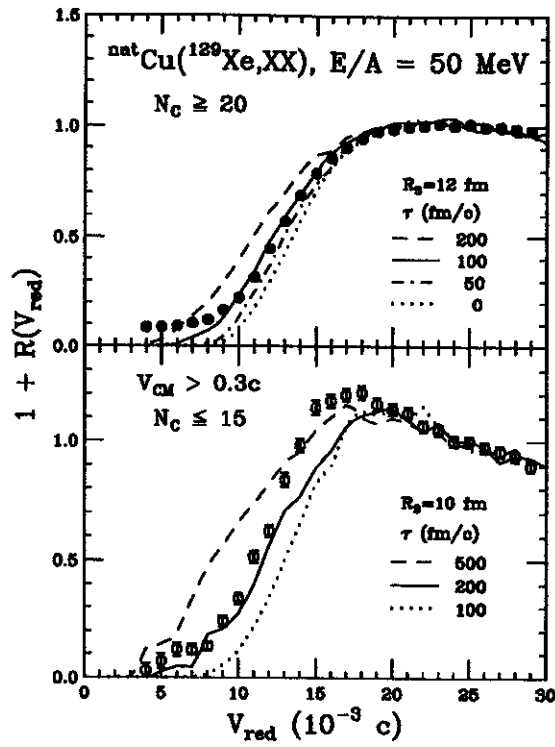
12

Figure 3: Comparison of experimental correlation functions (solid and open points) with three-body trajectory calculations (curves). The top panel shows results gated on high multiplicity events, the bottom panel results gated on low multiplicity events for fragments with a center-of-mass velocity >0.3c. The curves correspond to calculations with the indicated source radii, R_S, and mean emission times, τ.

fm/c. The data show best agreement with the simulation for $\tau=100$ fm/c. In Table 2, the reduced χ^2 values for these simulations, along with others for identical mean emission times and $R_S=10$ and 14 fm [8] are shown [9]. For any reasonable choice of radius parameter, the time scale for fragment emission in central collisions is ≤ 100 fm/c. These time scales are consistent with those extracted for central collisions in ^{36}Ar + ^{197}Au reactions at E/A = 35-110 MeV [1, 2].

We have varied the source velocity and source charge parameters to investigate the uncertainties in the results of the three-body simulations. The source velocity was varied between the nucleon-nucleon center-of-mass velocity (0.16c) and the beam velocity (0.33c). The source charge was varied between 0 and 83 (complete fusion). The sensitivity of the calculations to these parameters corresponds to an uncertainty in mean emission time of ≈ 50 fm/c.

The fragment velocity distributions indicate emission time scales for peripheral collisions long enough to allow the separation of the PLF and TLF, as predicted by the deep inelastic scattering and incomplete fusion mechanisms, but shorter than the rotational time of the excited PLF. Assuming a relative velocity equal to the beam velocity, the time required for the ^{129}Xe projectile to pass the ^{nat}Cu target is ≈ 70 fm/c. This time is a lower limit to the projectile-target separation time; any dissipation of the entrance channel kinetic energy will give a longer separation time. The time necessary for rotation of a ^{129}Xe nucleus with angular momentum of J=88$\hbar$ [10] is approximately 700 fm/c (smaller values of J will lead to correspondingly longer rotational times). As expected, the emission time of 200-500 fm/c extracted for high velocity fragments in peripheral collsions falls between the PLF-TLF separation time and the PLF rotational time.

The emission time scale of of ≤ 100 fm/c extracted for central collisions is similar to the separation

time of the PLF and TLF calculated above. This short time scale precludes PLF/TLF mechanisms such as deep inelastic scattering or incomplete fusion and accounts for the single apparent source in the observed velocity distributions.

In summary, we have compared fragment velocity distributions and fragment- fragment correlation functions for the ^{129}Xe + ^{nat}Cu reaction at E/A = 50 MeV. In peripheral collisions a projectile-like source exists which decays on a time scale long enough to allow separation from a target -like fragment, but of insufficient lifetime to allow complete equilibrium. Central collisions are characterized by broad, anisotropic velocity distributions and decay times too short to allow a separation of sources.

a. Chalk River Laboratories, Chalk River, Ontario K0J 1J0, Canada
b. Hope College, Holland, Mi 49423
c. Instituto de Fisica, Universidade de Sao Paulo, C. Postal 20516, CEP 01498, Sao Paulo, Brazil
d. Department of Chemistry and Indiana University Cyclotron Facility, Bloomington, IN 47405
e. Lawrence Berkeley Laboratory, Berkeley, CA 94720
f. Indiana University Cyclotron Facility, Bloomington, IN 47405
i. INFN - Sez. di Bari, 70126 Bari, Italy

References

1. Y.D. Kim et al., Phys. Rev. C45, 338 (1992).
2. D. Fox et al., Phys. Rev. C47, R421 (1993).
3. R.T. de Souza et al., Nucl. Instr. Meth. A295 109 (1990).
4. W.L. Kehoe et al., Nucl. Instr. Meth. 311 258 (1992).
5. B.V. Jacak et al., Phys. Rev. C35, 1751 (1987).
6. The distributions shown in Fig. 2 select peripheral collisions that are on average slightly more violent ($< N_c >= 13$) than the events leading to Z=2 ($< N_c >= 10$) or Z=6 ($< N_c >= 11.5$) emission shown in Fig. 1. The velocity distributions gated on two-fragment events are qualitatively similar to those shown in Fig. 1. For central collisions, all of the distributions shown in Figs. 1 and 2 select events with approximately the same average multiplicity ($< N_c >\approx 22$).
7. The theoretical and experimental correlation functions were normalized in the region $v_{red} >0.022c$.
8. For orientation, the distances between the centers of a ^{12}C fragment and the residues corresponding to a ^{129}Xe source (projectile) and a ^{193}Bi source (complete fusion), are 8.8 and 9.7 fm, respectively.
9. The reduced chi-squared values were determined from the ascending portions of the correlation functions, $0.01c \leq v_{red} \leq 0.020$ for high multiplicity events, and $0.008c \leq v_{red} \leq 0.015c$ for low multiplicity events.
10. The maximum angular momentum a ^{129}Xe nucleus can sustain with a nonzero fission barrier is 88 $\hbar$.

AZIMUTHAL CORRELATIONS AS A TEST FOR CENTRALITY IN HEAVY-ION COLLISIONS

L. Phair[a], D.R. Bowman[b], C.K. Gelbke, W.G. Gong[a], Y.D. Kim[c], M.A. Lisa[a], W.G. Lynch, G.F. Peaslee[d], R.T. de Souza[e], M.B. Tsang and F. Zhu[f]

Intermediate-energy nucleus-nucleus collisions may produce finite nuclear systems at temperatures and densities commensurate with a liquid-gas phase transition in infinite nuclear matter. Calculations indicate that many promising signatures are strongly influenced by the impact parameter[1]. Such dependencies are difficult to unravel in inclusive experiments because of the averaging over the impact parameter. Better comparison between experiment and theory can be made when one focuses on exclusive measurements where reaction filters are used to select narrow ranges of impact parameter. For studies addressing the thermodynamic properties of nuclear matter, the selection of central collisions is of particular interest since reaction zones formed in central collisions promise to reach the largest degree of equilibration.

Azimuthal correlations of particles emitted in collisions between ^{197}Au target nuclei and ^{36}Ar projectiles at E/A=35, 50, 80 and 110 MeV have been measured with the MSU Miniball[2]. We have tested various impact parameter filters by their ability to suppress the collective motion measured by the azimuthal correlations.

For this analysis the following quantities have been used to select the magnitude of the impact parameter:

(i) The charged-particle multiplicity, N_C, includes all charged particles detected.

(ii) The total transverse kinetic energy of identified particles is

$$E_t = \sum_i \frac{(p_i \sin \theta_i)^2}{2m_i} \tag{1}$$

where p_i, m_i and θ_i denote the momentum, mass and polar emission angle of particle i with respect to the beam axis.

(iii) The mid-rapidity charge, Z_y, is defined [3] as the summed charge of all identified particles of rapidity y (measured in the center of mass frame) with $0.75y_{target} < y < 0.75y_{projectile}$.

In order to construct an approximate impact parameter scale, we followed the geometric prescription [4] utilized previously [5]. For each of the quantities N_C, E_t and Z_y we assume a monotonic relationship to the impact parameter and define the reduced impact parameter scale

$$\frac{b(X)}{b_{max}} = \hat{b}(X) = \left(\int_X^\infty \frac{dP(X')}{dX'} dX' \right)^{1/2}, \tag{2}$$

where $X = N_C, E_t$ and Z_y; $dP(X)/dX$ is the normalized probability distribution for the measured quantity X and b_{max} is the maximum impact parameter for which particles were detected in the Miniball ($N_C \geq 2$). The reduced impact parameter scale $\hat{b}$ ranges from $\hat{b} = 1$ for glancing collisions to $\hat{b} = 0$ for head-on collisions.
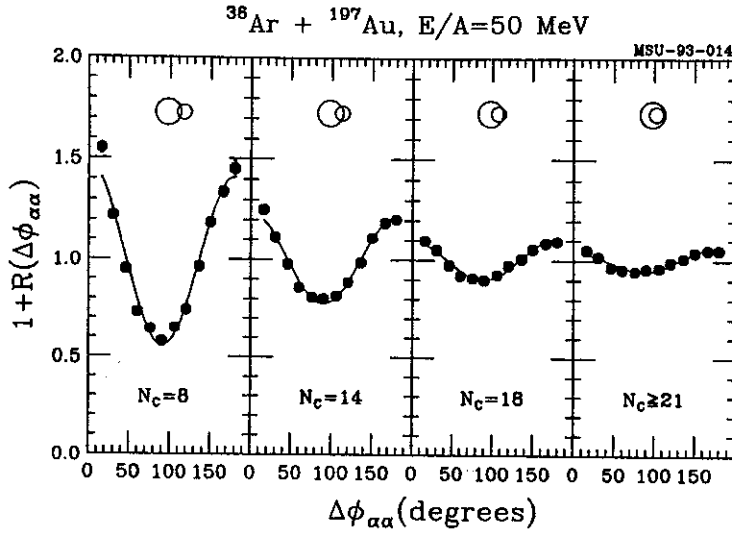
Figure 1: Azimuthal correlation functions for He nuclei emitted in ^{36}Ar+^{197}Au collisions at E/A=50 MeV. Panels from left to right show the data selected by cuts on reduced impact parameters $\hat{b}$=0.8, 0.6, 0.4 and <0.2, respectively; the actual cuts on charged particle multiplicity N_C are indicated in the figure. The circles show the approximate geometrical overlap between target and projectile for the different cuts in N_C.

In order to quantify the selection of collisions with small impact parameters, we explored the azimuthal correlations between emitted alpha particles. The azimuthal correlation function is defined by the ratio

$$\left.\frac{Y(\Delta\phi)}{Y'(\Delta\phi)}\right|_{\theta,\hat{b}} = C[1 + R(\Delta\phi)]|_{\theta,\hat{b}} \tag{3}$$

where $Y(\Delta\phi)$ is the coincidence yield of two (identical) particles emitted with relative azimuthal angle $\Delta\phi$ at a polar angle θ and in collisions selected by a specified cut on reduced impact parameter $\hat{b}$; $Y'(\Delta\phi)$ is the background yield constructed by mixing particle yields from different coincidence events, but selected by identical cuts on the reduced impact parameter; C is a normalization constant such that the average value of the correlation $1 + R(\Delta\phi)$ is one.

For truly central collisions, a reaction plane is undefined and the azimuthal distribution of emitted particles must be symmetric about the beam axis. If the azimuthal correlations between two emitted particles reflect their single-particle emission patterns, the azimuthal correlation function must become flat for central collisions. For peripheral collisions transverse-flow effects or other ordered motion in the reaction plane can cause large anisotropies in the azimuthal correlations. Figure 1 shows azimuthal correlation functions for He nuclei emitted in ^{36}Ar+^{197}Au collisions at E/A = 50 MeV. Different panels of the figure show results for different cuts on the charged-particle multiplicity N_C. For each panel, the overlapping circles present a simple geometric picture of the collision geometry deduced by means of equation (2). At large impact parameters, i.e. low values of N_C, the correlation functions show a strong preference of emission at relative azimuthal angles of $\Delta\phi \approx 0°$ and $180°$, characteristic of preferential emission in the reaction plane. At larger values of N_C, the azimuthal correlation functions become more isotropic.

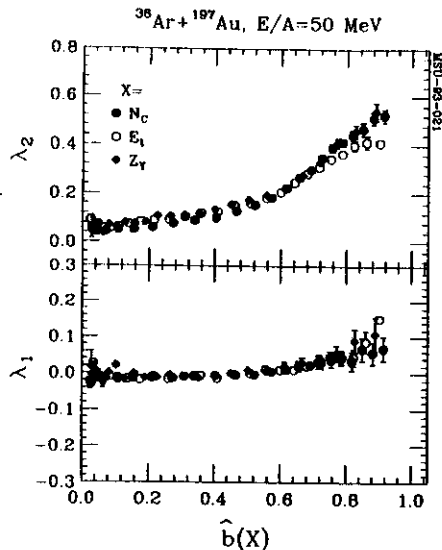In order to allow a more compact presentation of the main features of the observed azimuthal

16

Figure 2: Reduced-impact-parameter dependence of the coefficients λ_1 and λ_2 used to fit the measured azimuthal correlation functions of He-nuclei emitted in ^{36}Ar+^{197}Au collisions at E/A=50 MeV. Results from different impact parameters filters are shown by the different symbols indicated in the figure.

correlation functions, we have fit them by functions of the form

$$1 + \lambda_1 \cos(\Delta\phi) + \lambda_2 \cos(2\Delta\phi), \tag{4}$$

where λ_1 and λ_2 are treated as free parameters. Large values of λ_2 may be associated with collective motion resembling a rotation. Positive (negative) values of λ_1 indicate preferential emission of the particle pair to the same side (opposite sides) of the beam. Positive values of λ_1 can come from large final-state interactions (e.g. the decay of ^{8}Be$\rightarrow 2\alpha$) or, alternatively, from directed sideward flow. Negative values of λ_1 (preferred emission on opposite sides of the beam) may reflect phase-space constrains for small systems due to momentum conservation. For isotropic distributions $\lambda_1 = \lambda_2 = 0$.

Figure 2 summarizes the parameters λ_1 and λ_2 extracted as a function of reduced impact parameter $\hat{b}$ constructed from N_C, E_t and Z_y. These impact parameter filters select, as expected [5], classes of events characterized by very similar azimuthal distributions. For all filters, λ_2 decreases as a function of decreasing reduced impact parameter. Indeed, $\lambda_2 \rightarrow 0$ as $\hat{b} \rightarrow 0$ with rather good accuracy, indicating that small reduced impact parameters do select near-central collisions for which $R(\Delta\phi) \approx 0$ by necessity. In the lower panel λ_1 is nearly zero for reduced impact parameters $\hat{b} \leq 4$. For larger $\hat{b}$, λ_1 assumes small positive values. These can arise from the sequential decay of the particle unstable nucleus ^{8}Be.

As determined from the shape of azimuthal correlation functions, the three impact parameter scales provide equivalent event selection. Only for the most peripheral reactions, do some slight differences exist. Small discrepancies between different impact parameter filters for peripheral collisions are not surprising since the determination of large impact parameters must be associated with relatively large statistical and systematic uncertainties. The present findings are qualitatively consistent with the results of ref [5].

a. Lawrence Berkeley Laboratory, Berkeley, CA 94720
b. Chalk River Laboratories, Chalk River, Ontario K0J 1J0, Canada
c. National Laboratory for High Energy Physics, 1-1 Oho, Tsukuba, Ibaraki 305, Japan
d. Physics Department, Hope College, Holland, MI 49223
e. Indiana University Cyclotron Facility, Indiana University, Bloomington, IN 47405

f. Brookhaven National Laboratory, Upton, Long Island NY 11973

References

1. M.B. Tsang *et al.*, Phys. Rev. C 40, 1685 (1989).
2. R.T. de Souza *et al.*, Nucl. Instr. Meth. A295, 109 (1990).
3. C.A. Ogilvie *et al.*, Phys. Rev. C 40, 654 (1989).
4. C. Cavata *et al.*, Phys. Rev. C 42, 1760 (1990).
5. L. Phair *et al.*, Nucl. Phys. A458, 489 (1992).

THE ONSET OF NUCLEAR VAPORIZATION

M.B. Tsang, W.C. Hsi, W.G. Lynch, D.R. Bowman, C.K. Gelbke, M.A. Lisa, G.F. Peaslee, G.J. Kunde[a], M.L. Begemann-Blaich[c], T. Hofmann[a], J. Hubele[a], J. Kempter[c], P. Kreutz[c], W.D. Kunze[a], V. Lindenstruth[a], U. Lynen[a], M. Mang[c], W.F.J. Müller[a], M. Neumann[c], B. Ocker[c], C.A. Ogilvie[a], J. Pochodzalla[a], F. Rosenberger[c], H. Sann[a], A. Schüttauf[c], V. Serfling[c], W. Trautmann[a], A. Tucholski[h], A. Wörner[a], B. Zwieglinski[h]; the LAND Collaboration[a], G. Raciti[f], G. Imme[f], R. J. Charity[b], L.G. Sobotka[b], I. Iori[e], A. Moroni[e], R. Scardoni[e], A. Ferrero[e], L. Stuttge[d], A. Cosmo[d], and G. Peilert[i]

To investigate the evolution from multifragmentation towards vaporization for central $^{197}Au+^{197}Au$ collisions, thin 3 and 5 mg/cm^2 ^{197}Au targets were bombarded with ^{197}Au ions of E/A= 100, 250 and 400 MeV at the SIS facility at GSI. Three distinct detection arrays were combined in this experiment to provide a 4π multifragment detection capability well suited to the kinematical conditions of symmetric $^{197}Au+^{197}Au$ collisions. At polar angles of $14.5° \le \Theta_{lab} \le 160°$, charged particles were detected in 215 plastic scintillator - CsI(Tl) phoswich detectors of the Miniball/Miniwall Array[1]. Intermediate mass fragments (IMF's: Z=3-30) that penetrated the plastic-scintillator foils of the phoswich detectors were distinguished from light particles (Z $\le$ 2); particles were further identified by element for Z≤10 and isotopically for Z=1. For $25° \le \Theta_{lab} \le 160°$, 4 mg/cm^2 plastic scintillator foils were used; the thresholds for particle identification in these detectors were $E_{th}/A \sim 2$ MeV (3 MeV) for Z=3 (Z=10) particles, respectively. For $14.5° \le \Theta_{lab} \le 25°$, 8 mg/cm^2 plastic foils were used; the corresponding thresholds were $E_{th}/A \sim 2.5$ MeV (4.5 MeV) for Z=3 (Z=10) particles, respectively. (Lower energy particles were detected in these detectors, but not identified.) Beam rapidity fragments with $2 \le Z \le 79$, were detected with the Aladin spectrometer system[2], which covered $|\Theta_{lab}| \le 10°$ in the horizontal (bend) plane and $|\Theta_{lab}| \le 5°$ in the vertical plane. IMF's emitted to angles between the Aladin spectrometer and the Miniball/Miniwall were detected in 84 elements of a Si-CsI(Tl) array, each consisting of 300 μ thick Si and 6 cm thick CsI(Tl) detectors, with representative thresholds of Eth/A $\sim$ 7.5 MeV (14.5 MeV) for Z=3 (Z=10) particles, respectively. High energy Lithium ions (E/A $\ge$ 180 MeV) which punched through the CsI(Tl) crystals were not counted as IMF's because such ions could not be accurately distinguished from light particles[3].

The transition from multifragmentation to vaporization is manifested in the incident energy and impact parameter dependence of the IMF multiplicities. Fig. 1 shows the correlation between $<N_{IMF}>$, the mean IMF multiplicity measured in the combined arrays, and N_C, the total charge particle multiplicity detected in the Miniball/Miniwall, for the three incident energies. This dependence of $<N_{IMF}>$ upon N_C is largely a reflection of the dependence of both quantities upon the impact parameter. To unfold this dependence and allow quantitative comparisons with fragmentation models, we have assumed a monotonic dependence of the charged particle multiplicity N_C upon the impact parameter [4],

$$\hat{b} = \frac{b}{b_{max}} = \left[\int_{N_C(b)}^{\infty} dN_C \cdot P(N_C) \right]^{1/2} , \tag{1}$$

to assign a mean "reduced" impact parameter, $\hat{b}$, to each data point in Fig. 1. Here, $P(N_C)$ is the probability distribution for the charged particle multiplicity for $N_C \geq 4$, and b_{max} is the mean impact parameter with $N_C = 4$.
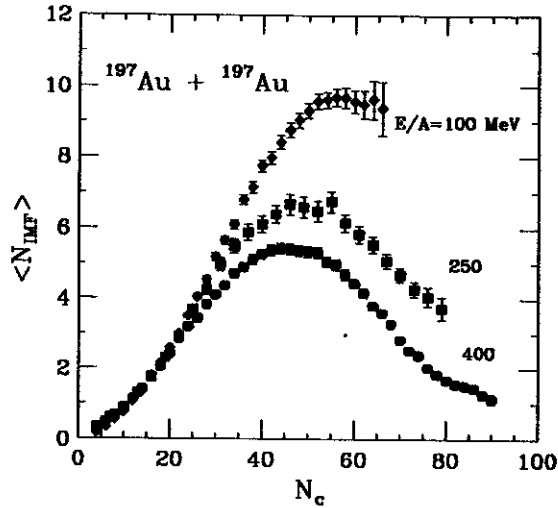

Figure 1: Correlation between $<N_{IMF}>$, the mean fragment multiplicity, and N_C, the multiplicity of charged particles detected in the Miniball/Miniwall, for $^{197}Au+^{197}Au$ collisions at $E/A = 100, 250, 400$ MeV.
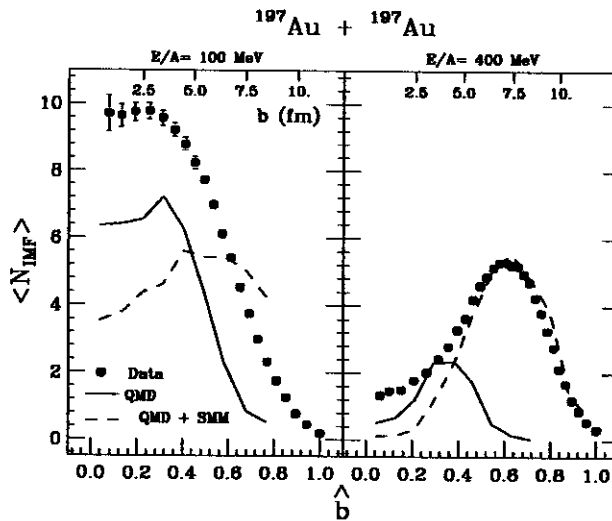

Figure 2: The measured impact parameter dependence of the mean fragment multiplicity is shown by the solid points. The solid lines depict the QMD calculations after filtering through the experimental acceptance. (QMD calculations are not presently available at E/A=250 MeV .) The open circles depict the predictions of the QMD-SSM models. The dashed lines depict the QMD-SSM hybrid model calculations after filtering through the experimental acceptance. The impact parameter scales are defined such that $\hat{b} = 1.0$ when b = 11.1 fm for E/A=100 MeV and $\hat{b} = 1.0$ when b=11.8 fm for E/A= 400 MeV.

Fig. 2 shows the mean IMF multiplicities as a function of $\hat{b}$. At E/A=100 MeV, $<N_{IMF}>$ is larger for small impact parameters than for large impact parameters, consistent with increased fragment production for collisions with increased compression and increased excitation energy. The mean multiplicity, $<N_{IMF}>$ ≈ 9-10, for central collisions is about 50% larger than the largest multiplicities previously observed[5,7]. Contrary to the impact parameter dependence observed at E/A = 100 MeV and the incident energy dependence observed at lower incident energies[7], however, the fragment multiplicities in central collisions do not increase with incident energy. Instead, a marked decrease in the fragment multiplicities is observed, consistent with the onset of vaporization in nuclear systems that are expanding too rapidly and are too highly excited to produce significant numbers of fragments. This trend is most striking at the highest incident energy, E/A=400 MeV, where multifragmentation is strongly suppressed for central collisions. For the more weakly excited systems produced in more peripheral collisions, multifragmentation persists and large fragment multiplicities, e.g. $<N_{IMF}>$ ≈ 5-6 for $\hat{b}$≈0.67 and E/A=400 MeV, are observed.

Over much of the incident energy domain spanned in this letter, both multifragmentation and collective flow have been successfully modeled for central collisions via microscopic molecular dynamics models[8-10]. It is interesting to explore whether such models can also describe the observed decline of multifragmentation for central collisions. The solid lines in Fig. 2 are the IMF multiplicities predicted by the microscopic quantum molecular dynamics (QMD) model of ref. [10]. After filtering through the experimental acceptance, the QMD model predicts significantly enhanced fragment multiplicities for central collisions at E/A = 100 MeV; these may be due to compression/rarefaction cycles traversed by the system during small impact parameter collisions[10.] It also predict a shift in the peaks of the fragment multiplicity distributions from small impact parameters at low energies to larger impact parameters at higher energies. The QMD calculations, however, significantly underpredict the measured peak IMF multiplicity at each incident energy, and strongly underestimate the shift in the peak fragment multiplicity with impact parameter.

Similar failures of QMD calculations to reproduce large IMF multiplicities observed at lower incident energies[7,6,11] and large impact parameters [12] have been attributed to an inadequate treatment of statistical fluctuations that lead to the statistical decay of highly excited reaction residues[11]. Such residues are also produced at b ≥ 4 fm in the present QMD simulations, and decay primarily by nucleon emission, *not by fragment emission* as predicted by statistical models[13]. The suppression of statistical fragment emission in QMD calculations is not fully understood, but it may be related to the classical heat capacities[11,14,15], the suppression of Fermi motion[11] and the neglect of quantum fluctuations within the hot residual nuclei as they are calculated within the QMD models.

To illustrate such statistical decay effects, we have taken the masses and excitation energies of bound fragments produced in the QMD calculations as the initial conditions for statistical model calculations. For these latter calculations, the decays of bound fragments were calculated via the statistical multifragmentation (SSM) model of ref. [17] which contains a "cracking" phase transition at low density. Input excitation energies and masses for the SSM model calculations were taken from the QMD calculations at an elapsed reaction time of 200 fm/c.

The dashed lines show the QMD-SSM prediction after the efficiency corrections for the experimental apparatus were applied. Including statistical decay increases the calculated peak fragment multiplicities at E/A=400 MeV to values comparable to the peak multiplicities calculated for central collisions at E/A=100 MeV. It also moves the peak fragment multiplicities to larger impact parameters, consistent with experimental observations. In central collisions, however, correcting for the sequential decay of hot intermediate mass fragments in the QMD-SSM hybrid model reduces the calculated fragment multiplicities significantly below the experimental values. This reduction becomes even more evident when such effects are calculated with the QMD-SSM model at E/A=100 MeV, see Fig. 2a. For such collisions, IMF's are either produced in insufficient

quantities by the QMD calculations or are too highly excited to survive the SSM statistical decay stage in numbers consistent with the experimental observations.

In summary, we have investigated ^{197}Au+^{197}Au collisions at E/A=100, 250 and 400 MeV with a large dynamic range 4π multifragment detection array. For central collisions at E/A=100 MeV, an average number of 10 intermediate mass fragments were detected, about 50% larger than the largest fragment multiplicities previously observed. The onset of nuclear vaporization with incident energy is observed; the IMF multiplicity is reduced to about 2 for central collisions at E/A=400 MeV and the peak IMF multiplicity is shifted to larger impact parameters. Interpretations of these multifragment decay configurations via microscopic molecular dynamics models generally underestimate the fragment yields and predict an incorrect impact parameter dependence for the IMF multiplicity at the highest incident energy. An improved description of peripheral collisions at the highest incident energy can be achieved by including the statistical decay of bound residues produced in the molecular dynamics simulations. Including such effects, however, worsens the agreement for central collisions.

a. Gesellschaft für Schwerionenforschung, D-64220,Darmstadt, Germany;
b. Department of Chemistry, Washington University, St. Louis, MO 63130, USA;,
c. Institut für Kernphysik, Universität Frankfurt, 60486 Frankfurt, Germany;
d. Centre de Recherches Nucléaires, Strasbourg, France;
e. I.N.F.N. and Dipartimento di Fisica, Università degli Studi di Milano, I-20133 Milano, Italy;
f. I.N.F.N. and Dipartimento di Fisica dell' Università, I-95129 Catania, Italy;
g. FZ Rossendorf, D01314 Dresden, Germany;
h. Soltan Institute for Nuclear Studies, Hoza 69, 00-681 Warsaw, Poland.
i. Lawrence Livermore National Laboratory, Livermore, CA 94550,

References

1. R.T. de Souza et al, Nucl. Instrum. Methods A **295**, 109 (1990); The Miniwall, a granular extension of the Miniball to forward scattering angles, uses technologies developed for the Dwarf Wall/Ball.
2. The ALADIN Collaboration GSI-Nachrichten-02-89 (1988).
3. Particles heavier than lithium, which punched through the CsI(Tl) detectors are distinguishable from light particles and counted as IMF's.
4. L.Phair et al, Nucl. Phys. **A548**, 489 (1992).
5. D.R. Bowman et al, Phys. Rev. **C46**, 1834 (1992).
6. D.R. Bowman et al, Phys. Rev. Lett. **67**, 1527 (1991).
7. R.T. de Souza et al, Phys. Lett. **B 268**, 6 (1991).
8. G. Peilert et al, Phys. Rev. **C 39**, 1402 (1989), and refs. therein.
9. D.H. Boal and J.N. Glosli, Phys. Rev. **C 38**, 1870 (1988).
10. G. Peilert et al, Phys. Rev. **C46**, 1457(1992), and refs. therein.
11. T.C. Sangster et al, Phys. Rev. **C46**, 1404 (1992).
12. C.A. Ogilvie et al, Phys. Rev. Lett. **67**, 1214 (1991).
13. L.P. Csernai and J. Kapusta, Phys. Rep. **131**, 223 (1986) and refs. therein.
14. William G. Lynch, Nucl. Phys. **A545**, 199c (1992).
15. D. H. Boal, J. N. Glosli, and C. Wicentowich, Phys. Rev. **C40**, 601 (1989).
16. J.P. Bondorf et al, Nucl. Phys. **A444**, 460 (1985); A.S. Botvina et al, Nucl. Phys. **A475**, 663 (1987).

COLLECTIVE EXPANSION IN CENTRAL AU+AU COLLISIONS

W.C. Hsi,G.J. Kunde[a], J. Pochodzalla[a], W.G. Lynch, M.B. Tsang, M.L. Begemann-Blaich[c], D.R. Bowman, R. J. Charity[b], A. Cosmo[d], A. Ferrero[e], C.K. Gelbke, T. Glasmacher, T. Hofmann[a], J. Hubele[a], G. Imme[f], I. Iori[e], J. Kempter[c], P. Kreutz[c], W.D. Kunze[a], V. Lindenstruth[a], M.A. Lisa, U. Lynen[a], M. Mang[c], A. Moroni[e], W.F.J. Müller[a], M. Neumann[c], B. Ocker[c], C.A. Ogilvie[a], G.F. Peaslee, G. Raciti[f], F. Rosenberger[c], H. Sann[a], R. Scardaoni[e], A. Schüttauf[c], C. Schwarz, W. Seidel[h], V. Serfling[c], L.G. Sobotka[b], L. Stuttge[d], W. Trautmann[a], A. Tucholski[h], C. Williams,A. Wörner[a], and B. Zwieglinski[h]

Recent experimental and theoretical evidence suggests a significant collective expansion [1-4] ocurring in heavy ion collision at intermediate energy, but little has been published to quantify the resulting collective radial flow. To investigate collective expansion in Au+Au collisions at E/A=100 MeV, thin ^{197}Au targets of 3 and 5 mg/cm^2 areal density were bombarded at the SIS facility of GSI by ^{197}Au ions of E/A= 100 and 400 MeV incident energy. Charged particles emitted to θ_{lab} = 14°-160° were detected in 215 plastic scintillator-CsI(Tl) phoswich detectors of the Miniball/Miniwall/ 4π Array [5]. Details of the experimental setup can be found in Ref. 6. Energy calibrations for Z=1 to 10 particles, accurate to 10%, were obtained by combining the "punch through" points measured in this experiment with detailed detector response functions measured at the NSCL K1200 Cyclotron of Michigan State University [7].

Radial flow effects should be enhanced for central collisions [8] selected. Assuming the charged particle multiplicity decreases monotonically with impact parameter, a "reduced" impact parameter, $\hat{b}$ =b/b$_{max}$, was determined following refs. [9,10]; here, b$_{max}$ was defined by <N$_C$(b$_{max}$)> = 4. Laboratory energy spectra for Boron fragments emitted in near central collisions ($\hat{b}$ < 0.33) are shown in Fig. 1; they display exponential slopes that become steeper with scattering angle. Such behavior is expected for symmetric systems due to their large center-of-mass (CM) velocity. Insufficient damping of the incident collective linear momenta of projectile and target due to transparency [10] or contributions from non-central collisions can result in additional elongations of the momentum distributions parallel to the beam axis. Such effects are well known, and can be well described at lower incident energies by a superposition of three isotropically emitting thermal sources corresponding to the decay of the participant region in addition to the decay of projectile- and target-like spectator nuclei [11,12].

The solid lines in the upper panel in Fig. 1 indicate best fits to the energy spectra assuming three relativistic Maxwellian distributions [13],

$$\frac{dP(\vec{p})}{dEd\Omega} = \sum_{i=1}^{3} \frac{dP_i(\vec{p})}{dEd\Omega} = \frac{dP_1}{dEd\Omega}(\vec{p}, \vec{V}_1, V_1) + \int_0^{2\pi} \frac{d\phi_R}{2\pi} \sum_{i=2}^{3} \frac{dP_i}{dEd\Omega}(\vec{p}, \vec{V}_i(\phi_R), V_i)$$ (1)

where E and $\vec{p}$ denote the kinetic energy and momentum of the emitted particle; $\vec{V}_i$ denotes the velocity and V_i the effective Coulomb barrier of the ith source; ϕ_R denotes the azimuthal angle of the reaction plane [14]. Here $\frac{dP_i}{dE \, d\Omega}(\vec{p}, 0, V_i)$ is defined in the rest frame of the source ($\vec{V}_i \equiv 0$) by

$$\frac{dP_i}{dE \, d\Omega}(\vec{p}, 0, V_i) = a_i \cdot \Theta(E - V_i)(E + mc^2 - V_i)\sqrt{(E + mc^2 - V_i)^2 - m^2c^4} \exp\left(-\frac{E - V_i}{T_i}\right)$$ (2)

and $\dfrac{dP_i}{dE\,d\Omega}(\vec{p},\vec{V}_i,V_i)$ is obtained from Eq. 2 by Lorentz transformation. In Eq. 2, a_i is a normalization constant, T_i is the temperature of the Maxwellian source, and $\Theta\!\left(E-V_i\right)$ is the unit step function. The mass m was taken to be that of the most abundant natural isotope, e.g. A=11 for Boron. Because of symmetry, we required in the CM frame $\vec{V}_3 = -\vec{V}_2$, $a_3 = a_2$, and T3 = T2. The fit parameters are given in Table 1. The transverse velocity for the spectator sources (i=2,3) were determined from fits to triple differential cross sections measured with respect to the reaction plane [15]. Reasonable variations of this velocity component influence little the parameters of the participant source.
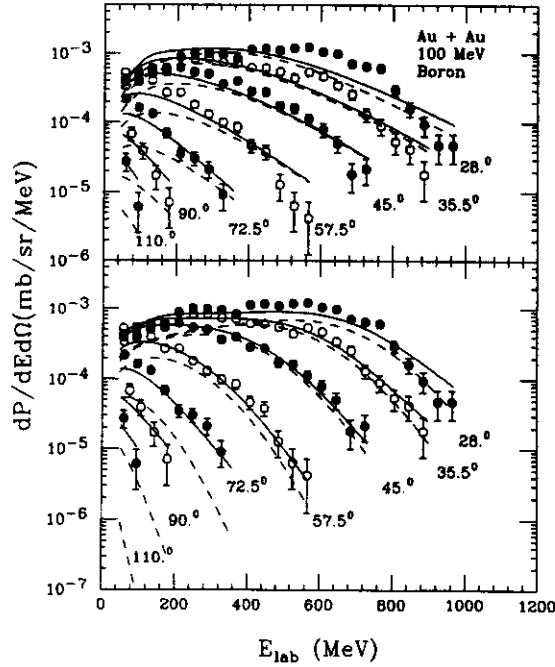

Figure 1: Comparisons of the energy spectra for Boron fragments emitted to Q_{lab}=28°, 35.5°, 45°, 57.5°, 72.5°, 90° and 110° (solid points) with corresponding moving source fits. Upper Panel: The solid lines correspond to fits obtained with Eq.1 and no radial expansion. Lower panel: The solid lines correspond to fits obtained with Eqs. 1 and 4, incorporating a radial expansion. The dashed lines in both panels correspond to the respective contributions from the participant sources alone.

Table 1. Parameters for three source fits. (Note: Fits 1 and 2 are without and with expansion, respectively, and the units for a_i, T_i and V_i are ($\mathrm{MeV^{-2.5} \cdot sr^{-1}}$), MeV, and MeV, respectively.)

Fit	Source	a_i	T_i	$v_{x,i}/c$	$v_{z,i}/c$	V_i	b_{exp}
1	1	9.2×10^{-11}	73.	0	0	35.	0
	2	3.2×10^{-11}	49.5	0.02	0.1	13.	0
2	1	1.1×10^{-9}	13.	0	0	0	0.16
	2	3.7×10^{-11}	59.	0.02	0.1	13.	0

To determine whether the discrepancy between fitted and measured spectra in the upper panel of Fig. 1 can be explained by a collective radial flow, a self similar radial expansion, $\vec{V}(\vec{r}) = c\beta_{exp}\vec{r}/R_S$, of the spherical participant source (i=1 in Eq. 1) was assumed which attains its maximum velocity $c\beta_{exp}$ at the surface $r = R_S$. The velocities of individual particles were assumed to be thermally distributed about the local radial expansion velocity with temperature T_1. Coulomb expansion after breakup was modeled in the limit of large β_{exp}, i.e. particles with charge Z_f, emitted from a source with charge Z_S, were aasumed to gain the kinetic energy $\Delta E_{Coul}(r) = Z_f(Z_S - Z_f)e^2 r^2/R_S^3$, without changing their direction. In the CM frame one obtains

$$\frac{dP_1}{dEd\Omega} = \frac{3}{4\pi R_S^3}\int_0^{R_S} r^2 dr \int d\Omega_r \int dE' \frac{dP_1}{dE'd\Omega}(\vec{p}',\vec{V}(\vec{r}),0)\delta\left(E'-E+\Delta E_{Coul}(r)\right), \quad (4)$$

where the direction of the particle's momentum is assumed to be unchanged. The total energy spectrum is obtained by inserting Eq. 4 into Eq.1 as the participant source.
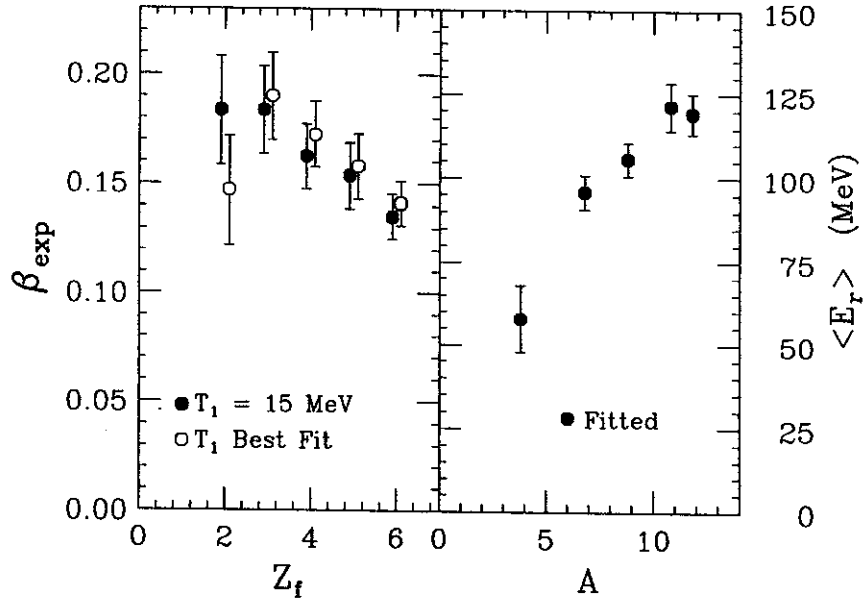

Figure 2: Left Panel: The open points correspond to best fit values for the radial expansion velocities as a function of the fragment charge. The solid points are the corresponding values obtained when T_1 is constrained to be 15 MeV. Right Panel: The solid points depict the dependence of the mean radial collective energy $\langle E_r \rangle$ extracted from the fits upon the fragment charge. The mass of the most abundant stable isotope is used.

Energy spectra for $Z_f = 2 - 6$ have been fitted using Eq. 4 and a non-zero radial expansion. Best fits, assuming $Z_S = 118$ and $R_S = 10$ fm, are shown by the solid lines in the lower panel of Fig. 1; they accurately follow the curvature in the energy spectra at $28° \leq q_{lab} \leq 57.5°$ where the participant source dominates. Extracted values for β_{exp} are not very sensitive to the spectral temperature T_1. They change by about $\pm 10\%$ as T_1 varies over the range 5 MeV $\leq T_1 \leq$ 20 MeV over which reasonable fits were obtained. Values of β_{exp}, extracted for different values of Z_f, are shown in the left panel of Fig. 2; they are similar when T_1 is varied freely (open points) or is held fixed (solid points) at $T_1 = 15$ MeV. Somewhat smaller radial expansion velocities are observed for

heavier fragments. Values for β_{exp} are not significantly changed by making a more restrictive gate, $\hat{b} < 0.16$, on the impact parameter.

Since β_{exp} and the Coulomb expansion dynamics have a similar influence on the energy spectra, there is a $\pm 3\%$ variation in β_{exp} with the breakup density over the interval $r = 0.1\text{-}0.3r_0$. This latter sensitivity is largely absent in the mean total radial collective energy defined by $\langle E_r \rangle = \frac{3}{5}\left(\frac{1}{2}mc^2\beta_{exp}^2 + Z_f(Z_s - Z_f)e^2 R_s\right)$, shown as the solid points in the right panel of Fig. 2. A linear increase in $\langle E_r \rangle$ with mass (charge) is observed for $Z_f \leq 4$, consistent with a uniform participation of these lighter fragments in the radial expansion. Heavier fragments with $Z_f \geq 5$ do not follow this trend as clearly.

In summary, energy spectra for IMF's produced in central Au+Au collisions at E/A = 100 MeV indicate a radial collective expansion at breakup. Values ranging from E_r/A = 10-15 MeV, extracted for the radial expansion energy decrease somewhat with the fragment charge.

a. Gesellschaft für Schwerionenforschung, D-64220,Darmstadt, Germany
b. Department of Chemistry, Washington University, St. Louis, MO 63130
c. Institut für Kernphysik, Universität Frankfurt, 60486 Frankfurt, Germany
d. Centre de Recherches Nucléaires, Strasbourg, France
e. I.N.F.N. and Dipartimento di Fisica, Università degli Studi di Milano, I-20133 Milano, Italy
f. I.N.F.N. and Dipartimento di Fisica dell' Università, I-95129 Catania, Italy
g. FZ Rossendorf, D01314 Dresden, Germany
h. Soltan Institute for Nuclear Studies, Hoza 69, 00-681 Warsaw, Poland

References

1. S.G. Jeong et al, report GSI-93-28.
2. H.W. Barz et al., Nucl. Phys. A531, 453 (1991).
3. W.Bauer et al., Phys. Rev. C47, 1838 (1993).
4. R.T. de Souza et al., Phys. Lett. B300, 29 (1993).
5. R.T. de Souza et al., Nucl. Inst. Meth. A 295, 109 (1990). The Miniwall, a granular extension of the Miniball to forward scattering angles, uses technologies developed for the Dwarf Wall/Ball.
6. M.B. Tsang et al., Phys. Rev. Lett. 71, 1502 (1993).
7. C. Schwarz et al., NSCL Annual Report (1994).
8. Q. Pan and P. Danielewicz, Phys. Rev. Lett. 70, 2062 (1993)
9. Y.D. Kim et al., Phys. Rev. C45, 338 (1992).
10. J.P Bondorf et al., Nucl. Phys. A333, 285 (1980).
11. L. Phair et al., Nucl. Phys. A548, 489 (1992).
12. R. Trockel, Prog. Part. Nucl. Phys. 15, 225 (1985).
13. L.D. Landau and E.M. Lifshitz, Statistical Physics 3d Edition Part 1, Pergammon Press (1980).
14. Azimuthal averaging can be neglected for the participant source (i=1) because its source velocity is directed along the beam and in special cases for the spectator sources (i=2,3) when one is dealing with triple differential cross sections where the azimuthal orientation of the reaction plane is known.
15. W.C. Hsi, to be published.

DETECTING MULTIFRAGMENT DISINTEGRATION OF NON-SPHERICAL BREAKUP GEOMETRIES

T. Glasmacher, C.K. Gelbke and S. Pratt

Microscopic calculations based upon the Boltzmann-Uehling-Uhlenbeck (BUU) transport theory predict [1-4] that ring-, disk- or bubble shaped nuclear configurations may be produced in the aftermath of central collisions between two heavy nuclei at suitably chosen incident energies. These structures are expected to undergo multifragment disintegrations. For example, formation and multifragment breakup of ring-shaped density distributions were predicted [2] for central ($b/b_{max} \leq$ 0.2) Nb + Nb collisions at incident energies between $E/A \approx 50$ and 80 MeV. The existence of such configurations has not yet been confirmed by experimental observation.

We suggest that information about the breakup geometry may be derived from fragment-fragment correlation functions, which depend on the relative location of the emitted particles. Multifragment disintegrations were simulated for spherical, disk- and ring-shaped source geometries by calculating the multibody Coulomb final state interactions between fragments emitted from schematic sources. The simulations are described in detail in ref. [5].
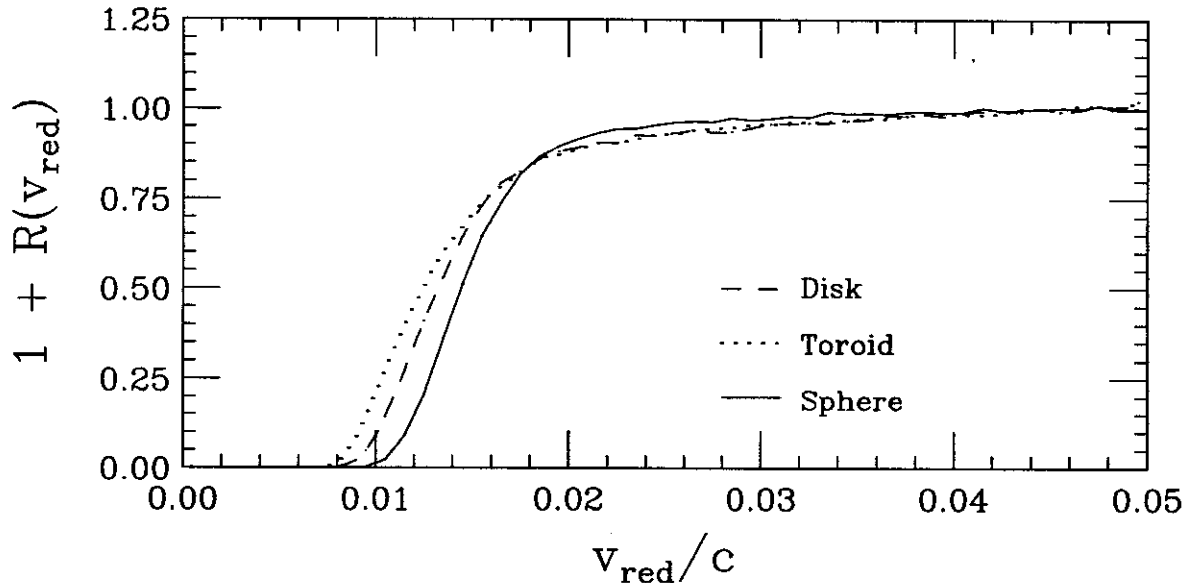

Figure 1: Comparison of angle-integrated two-fragment ($3 \leq Z \leq 20$) correlation functions for three different breakup geometries.

Two fragment correlation functions $1+R(v_{red})$ were defined as

$$1 + R(v_{red}) = C \cdot \frac{\sum Y_2(p_1, p_2)}{\sum Y_b(p_1, p_2)},$$

(1)

where $Y_2(p_1, p_2)$ is the calculated two-particle coincidence yield; $Y_b(p_1, p_2)$ is the background yield obtained by event mixing, i.e. by taking particles 1 and 2 from different events; and v_{red} is the "reduced" relative velocity,
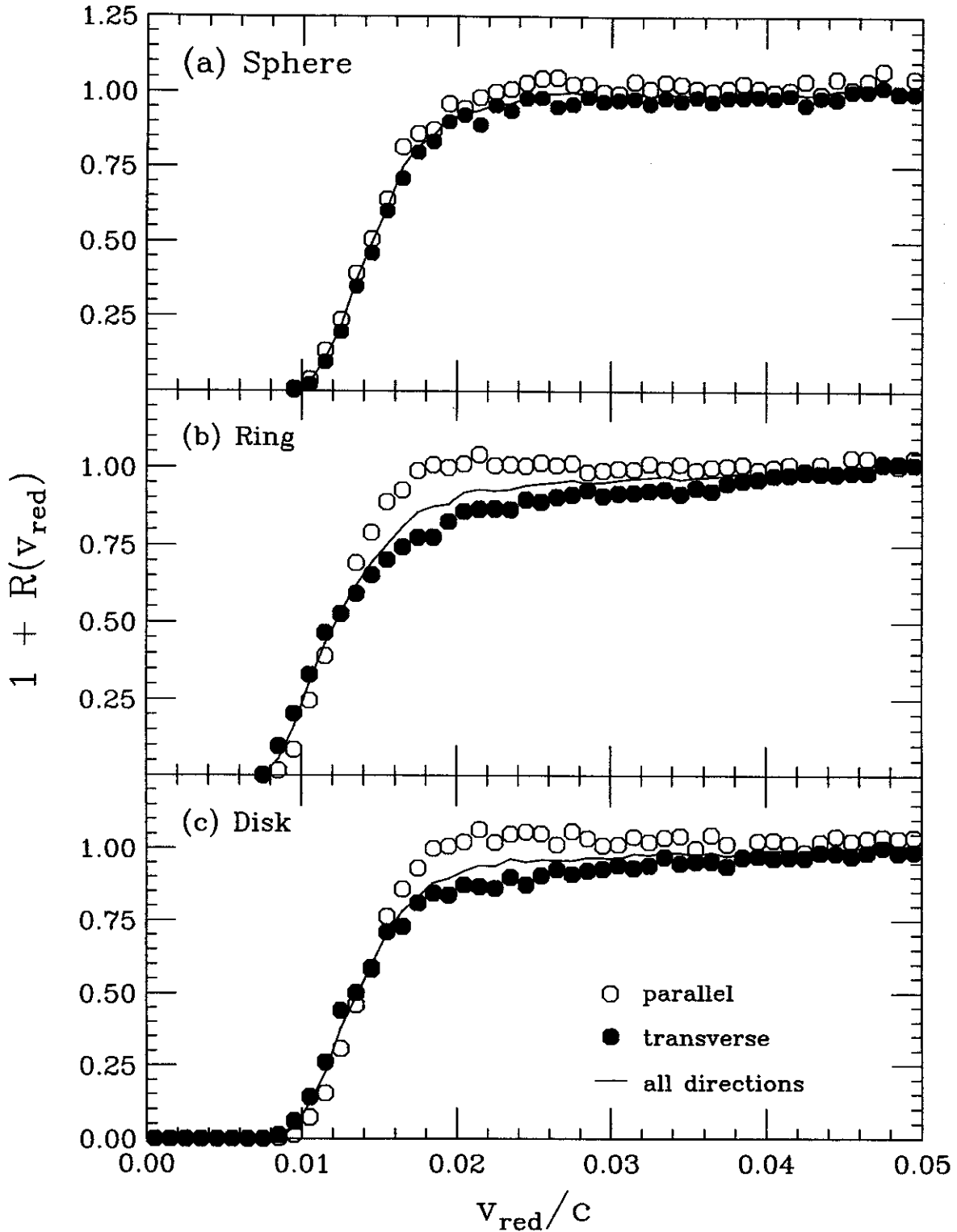
Figure 2: Parallel ($|\hat{\mathbf{v}}_{rel} \cdot \hat{z}| \geq 0.75$, open circles), transverse ($|\hat{\mathbf{v}}_{rel} \cdot \hat{z}| \leq 0.25$, filled circles), and angle-integrated two-fragment correlation functions (solid line) for (a) spherical, (b) toroidal and (c) disk-shaped breakup geometries constructed from light intermediate mass fragments ($3 \leq Z \leq 8$) selected by a cut on the direction of the total momentum of the fragment pairs corresponding to $|\hat{\mathbf{P}} \cdot \hat{z}| \geq 0.75$. The statistical error bars are smaller than the symbols.

$$V_{red} = \frac{V_{rel}}{\sqrt{Z_1 + Z_2}} \qquad (2)$$

which accounts for the scaling of the correlation function for different types of fragments. In eq. (1), the sums extend over all particle momenta corresponding to a given bin of v_{red} and to other specified cuts - for example the direction of v_{red} or the magnitude and direction of the total momentum $P = p_1 + p_2$. The normalization constant C is determined by the normalization condition $<R(v_{red})> = 0$ where the average is taken over the interval $0.04 \text{ c} \leq v_{red} \leq 0.05 \text{ c}$.

Correlation functions calculated for the three different break-up geometries, but unconstrained by directional cuts, are presented in fig. 1. As expected, these correlation functions exhibit little sensitivity to the shape of the emitting system. In our particular example, the ring and disk-shaped configurations are less compact than the spherical configuration. For these less compact systems, the average distance between emitted particles is larger, and the average Coulomb interaction between the emerging particles is reduced. As a consequence, the minimum of the correlation functions at $v_{red} \approx 0$ is slightly narrower. However, the overall shapes of the correlation functions are very similar. Since the width of the minimum at $v_{red} \approx 0$ depends on the (unknown) size of the emitting system, a distinction of different source shapes by means of such angle integrated correlation functions would be virtually impossible.

Directional dependences of two-fragment correlation functions might provide information about non-spherical breakup configurations. Such directional dependences originate from the Coulomb interaction which acts along the relative coordinate of the two detected particles. These dependences are shown in fig. 2. The directional cuts applied in the evaluation of the correlation functions were defined in terms of the angle between the relative fragment velocity ($\hat{v}_{rel} = v_{rel}/|v_{rel}|$) and the symmetry ($\hat{z}$) axis. Parallel ($|\hat{v}_{rel} \cdot \hat{z}| \geq 0.75$) and transverse ($|\hat{v}_{rel} \cdot \hat{z}| \leq 0.25$) correlation functions are sensitive to the source geometry. Only lighter fragments ($3 \leq Z \leq 8$) were used in this analysis, and emission along the symmetry axis was enhanced by the cut $|\hat{P} \cdot \hat{z}| \geq 0.75$, where $\hat{P} = P/|P|$ is the unit vector along the direction of the total momentum, $P = p_1 + p_2$, of the two detected fragments. For spherical sources of negligible lifetime, parallel and transverse correlation functions are, as expected, very similar, see Fig. 2a. (Some minor differences may be caused by final-state interactions with other particles.) Ring- and disk-shaped distributions, on the other hand, produce rather different parallel and transverse correlation functions, an effect which can be measured without much difficulty. This qualitative difference is sensitive to the shape of the source. It allows a clear distinction of spherical sources from ring- and disk-shaped sources, but it does not provide a distinction between ring- and disk-shaped geometries. Such more subtle differences in source geometries appear to be very difficult to establish by experimental observation.

References

1. L. G. Moretto et al., Phys. Rev. Lett. 69 (1992) 1884.
2. W. Bauer, G. F. Bertsch and H. Schulz, Phys. Rev. Lett. 69 (1992) 1888.
3. D.H.E. Gross, B.A. Li and A.R. DeAngelis, Ann. Physik 1 (1992) 467.
4. B. Borderie, B. Remaud, M.F. Rivet and F. Sebille, Phys. Lett. B302 (1993) 15.
5. T. Glasmacher, C.K. Gelbke and S. Pratt, Phys. Lett. B314 (1993) 265.

FRAGMENT-FRAGMENT CORRELATION FUNCTIONS WITH DIRECTIONAL EMISSION CUTS FOR CENTRAL ^{36}Ar+^{197}Au REACTIONS AT E/A=50 MeV

T. Glasmacher, L. Phair[a], D.R. Bowman[b], C.K. Gelbke, W.G. Gong[a], Y.D. Kim[c], M.A. Lisa[a], W.G. Lynch, G.F. Peaslee[d], R.T. de Souza[e], M.B. Tsang, and F. Zhu[f]

The emission of intermediate mass fragments (IMF) has been established as a decay mechanism of excited nuclear matter at high [1] and intermediate bombarding energies [2]. Some statistical treatments [3] are based upon the assumption of a nearly instantaneous fragmentation of an excited nuclear system at low density. Other models are based upon the assumption of a sequential decay mechanism from a hot and possibly expanding nuclear system undergoing equilibration between the individual binary disintegration steps [4]. Measurements of source dimensions and emission time scales can help determine which of these two extreme scenarios (if any) may be more realistic for the description of multifragment disintegrations. Two-fragment correlations are sensitive to the space-time extend of the emitting source and can provide such information. They can be treated in terms of classical Coulomb trajectory calculations since the deBroglie wavelengths of the emitted particles are short and since final-state interactions are dominated by the long–range Coulomb interaction [5]. Most analyses of two-fragment correlation functions employed correlation functions integrated over all angles between the total and relative momentum vectors of the emitted fragments (compatible with a given detector acceptance) [5-11]. Such "angle-integrated" correlation functions cannot resolve certain ambiguities between source size and lifetime. Since fragment emission is believed to be enhanced if the systems can expand to subnormal density, the size of the fragment emitting source is unknown. Hence, the extracted lifetimes depend upon the assumed source size. In this paper, we will show that studies of longitudinal and transverse correlation functions may help reduce such ambiguities and we apply this technique to a reinvestigation of two-fragment correlation functions measured for the reaction ^{36}Ar + ^{197}Au at E/A = 50 MeV. A detailed description of the experiment can be found in ref. [12].

Near-central collisions of ^{36}Ar + ^{197}Au at a beam energy of E/A = 50 MeV were selected by cuts on the observed charged particle multiplicity, $N_C \geq 19$. This centrality cut corresponds to a reduced impact parameter of $b/b_{max} \leq 0.3$, and it represents less than 10% of the reaction cross section. The average multiplicity of detected intermediate mass fragments in these central collisions was close to two. Fragments emitted below the Coulomb barrier ($E_{lab}/A \leq 6$ MeV) were excluded from this analysis.

Small angle correlation functions, $1+R(v_{red})$, were constructed for pairs of intermediate mass fragments ($4 \leq Z_{IMF} \leq 9$), detected at angles between $16° \leq \theta_{lab} \leq 40°$ in the laboratory frame. The correlation function was defined as

$$1 + R(v_{red}) = C \frac{\sum Y_{12}(p_1, p_2)}{\sum Y_{back}(p_1, p_2)}, \qquad (1)$$

where $Y_{12}(p_1, p_2)$ is the measured coincidence yield and $Y_{back}(p_1, p_2)$ is the "background yield" constructed via the event mixing technique. In eq. (1), p_1 and p_2 denote the laboratory momenta of the fragments 1 and 2, and v_{red} is the relative velocity of the particle pair defined as

$$v_{red} = \frac{v_{rel}}{\sqrt{Z_1 + Z_2}} = \frac{p_1/m_1 - p_2/m_2}{\sqrt{Z_1 + Z_2}}. \qquad (2)$$

Longitudinal and transverse cuts were defined by $\psi_{long} = 0°\text{-}50°$ and $\psi_{trans} = 80°\text{-}90°$, respectively. The angle $\psi = \cos^{-1}[|\mathbf{P'}.\mathbf{v}_{red}|/(\mathbf{P'} v_{red})]$ is defined as the angle between the reduced relative velocity vector, v_{red}, and the total momentum vector, $\mathbf{P'} = \mathbf{p'_1} + \mathbf{p'_2}$, of the coincident fragment pair, defined the rest frame of an assumed source moving with a fixed velocity v_ψ parallel to the beam axis.

Experimental correlation functions are shown in fig. 1. For simplicity, the directional cuts were defined close to the center-of-mass frame, $v_\psi = 0.04c$. The longitudinal correlation function (open squares) exhibits a substantial change in shape and height at larger reduced velocities, $v_{red}/c \approx 0.02$ - 0.05, compared to the angle integrated (solid circles) and transverse (open diamonds) correlation functions.

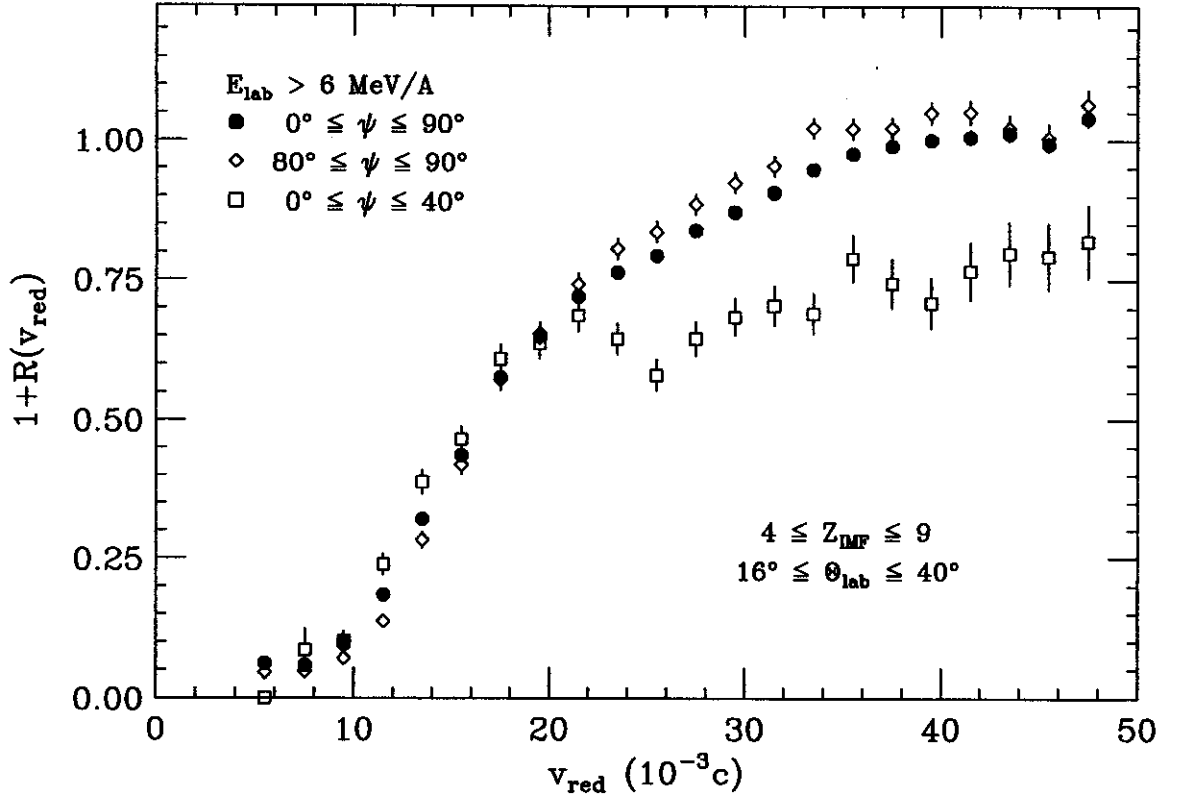Figure 1: Measured angle-integrated fragment-fragment correlation functions for charges ($4 \leq Z_{IMF} \leq 9$) emitted in central ^{36}Ar + ^{197}Au collisions ($b/b_{max} \leq 0.3$) at E/A = 50 MeV. The correlation functions are shown for fragments detected at forward angles ($16° \leq \theta_{lab} \leq 40°$). Energy thresholds of $E_{th} > 6$ MeV/A are applied to each fragment in the laboratory frame. Angle-integrated correlation functions ($\psi_{long} = 0°$ - 90°) are shown in solid circles. Longitudinal (squares) and transverse (diamonds) correlation functions correspond to $\psi_{long} = 0°$ - 40° and $\psi_{trans} = 80°$ - 90° measured in a rest frame of velocity $v_\psi = 0.04c$.

To extract size and lifetime parameters of emission sources consistent with the experimentally observed correlation functions, we simulated the final state interactions between the emitted fragments in terms of many-body trajectory calculations. For this purpose, the intermediate mass fragments were assumed to be sequentially emitted from the surface a spherical source and their final momenta under their mutual Coulomb interaction were calculated by numerically integrating Newton's equations of motion. Charge, energy and angular distributions of the emitted fragments ($4 \leq Z_{IMF} \leq 9$) were selected by randomly sampling the experimental yields. A detailed description of the simulations can

be found in ref. [13]. These events were filtered for the geometrical acceptance, granularity, and energy thresholds of the MSU Miniball. The simulated and filtered events were then treated in exactly the same way as the measured data, and correlation functions were constructed as described above.

Two-fragment correlation functions are sensitive to the strength of the final–state Coulomb interaction between the emitted fragments and also to the strength of the Coulomb interaction between emitted fragments and the residual source [5]. Details of these final-state interactions depend on the source size and on the time-scale of fragment emission. In general, the correlations are reduced (i.e. the width of the minimum in the correlation function at $v_{red} \approx 0$ becomes smaller) when the average separation between the emitted fragments becomes larger, as is the case for emission from larger sources or at larger time-intervals. While angle-integrated two-fragment correlation functions are sensitive to the space-time characteristics of the emitting system, they are poorly fit to distinguish between emission from larger, but short-lived sources as opposed to emission from small, but longer-lived sources. This ambiguity is illustrated more clearly in fig. 2. Four different combinations of radius and lifetime, ranging from $(R_S, \tau) = (10 \text{ fm}, 10 \text{ fm/c})$ to $(R_S, \tau) = (5.5 \text{ fm}, 100 \text{ fm/c})$, predict virtually indistinguishable angle-integrated two-fragment correlation functions. Hence, for the present source parametrization, the accuracy of lifetime determination is limited by uncertainties of the source radius. In spite of this ambiguity, the measured correlation function indicates a short emission time scale, $\tau \leq 100 \text{ fm/c}$, for all reasonable source dimensions, thus corroborating the conclusions reached by previous analyses [5-8,10] of multifragment emission processes at comparable energies.
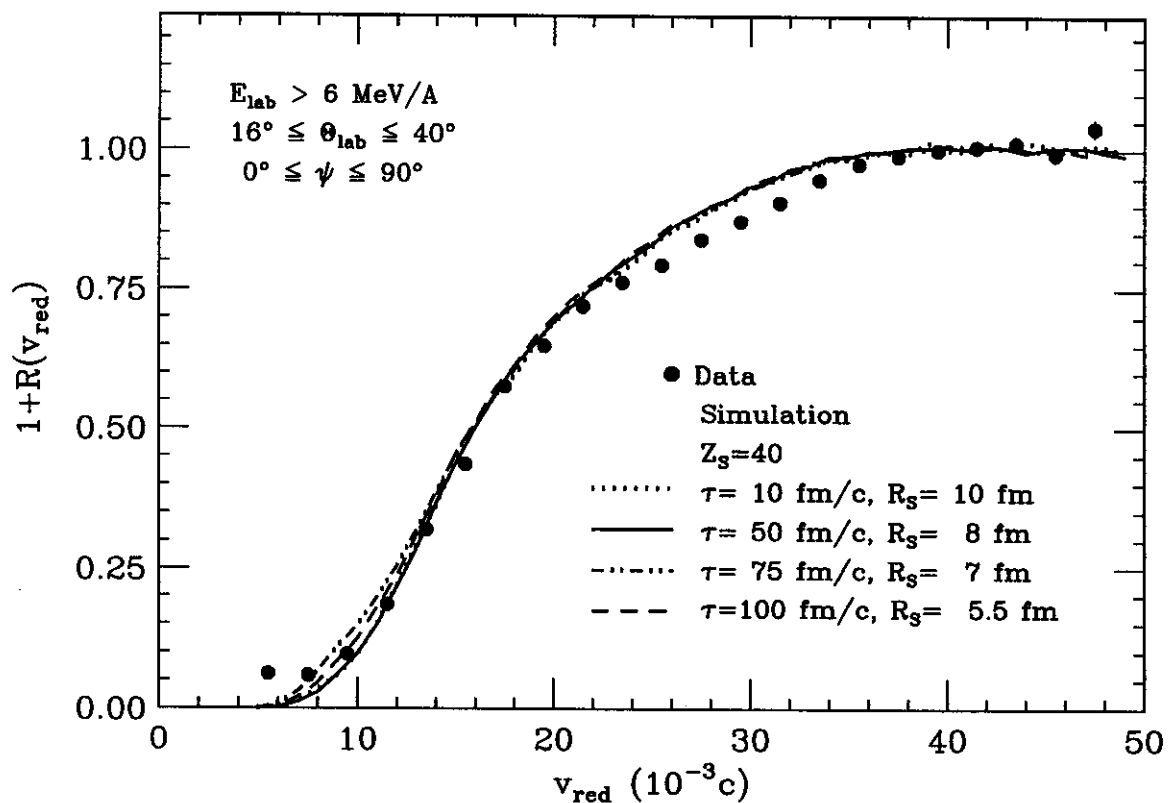

Figure 2: Angle-integrated correlation functions simulated via many-body Coulomb trajectory calculations for different combinations of source lifetimes τ and radii R_S (lines) are virtually indistinguishable. The measured correlation function is shown in by solid points. The simulations are filtered for acceptance, detector granularity, and energy thresholds.

The space-time ambiguity can be reduced by employing directional cuts in the construction of the two-fragment correlation function which are more sensitive to the mutual interactions between the two detected fragments and the emitting source, i.e. by constructing correlation functions for pairs of fragments with their relative velocity mainly parallel or transverse to their total momentum vector.

Measured (solid points) and calculated (curves) longitudinal two-fragment correlation functions are compared in fig. 3. The calculations illustrate that longitudinal correlation functions are non-degenerate for the same sets of parameters from fig. 2 which produced nearly indistinguishable angle-integrated correlation functions. This suggests that simultaneous investigation of angle-integrated and directional correlation functions can reduce the ambiguities encountered in the interpretation of angle-integrated correlation functions alone. (Transversal correlation functions display much less sensitivity and are not shown here.) With increasing lifetime, the calculated longitudinal correlation function becomes flatter for $0.01 \leq v_{red}/c \leq 0.03$, and then exhibits a more gradual rise towards unity at larger values of v_{red}. (While the longitudinal correlation functions do not reach unity for the reduced velocity range plotted here, we have verified that they do approach unity for larger reduced velocities, $v_{red} \approx 0.1c$.)

The experimental data fall within the range spanned by the simulations and agree best with the calculations for $(R_S, \tau) = (8 \text{ fm}, 50 \text{ fm}/c)$, indicating fragment emission on a fast time scale and from a rather large source. We have checked that these simulations are stable with respect to variations in uncertain model assumptions and parameters [13].
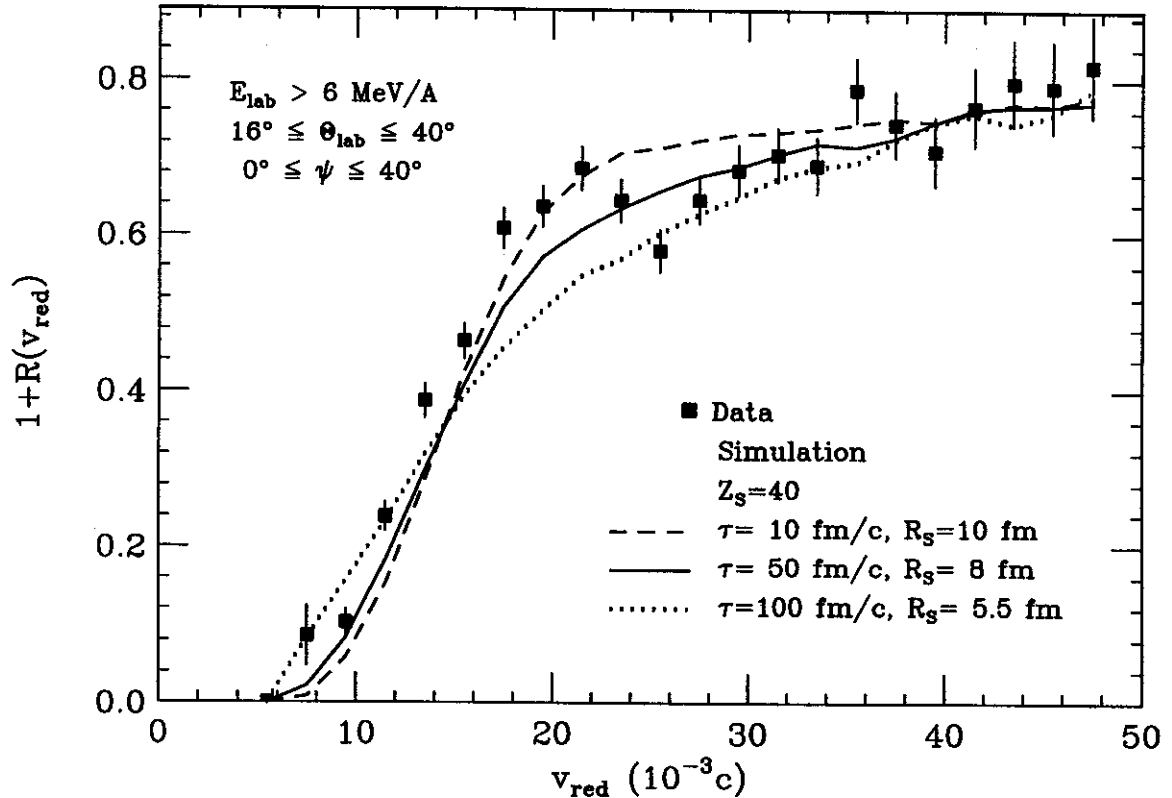

Figure 3: Longitudinal correlation functions ($\psi = 0^\circ - 40^\circ$) reduce the ambiguities shown in fig. 2.

Angle-integrated correlation functions were shown to exhibit significant ambiguities with regard to the spatial (R_S) and temporal (τ) extend of the reaction zone, with nearly equivalent corre-

lation functions being predicted for emission from a large but short-lived source ($R_S = 10$ fm, $\tau = 10$ fm/c) and a small but longer lived source ($R_S = 5.5$ fm, $\tau = 100$ fm/c). This ambiguity is reduced for longitudinal correlation functions. A consistent description of both angle-integrated and longitudinal correlation functions extracted from central collisions in ^{36}Ar+^{197}Au at E/A=50 MeV could be achieved by assuming emission on a fast time scale from the surface of an extended spherical source. The extracted average time for the emission of all fragments is $\tau \approx 50$ fm/c with a corresponding radius of $R_S \approx 8$ fm.

a. Lawrence Berkeley Laboratory, Berkeley, CA 94720.
b. Chalk River Laboratories, Chalk River, Ontario K0J1J0, Canada.
c. Indiana University Cyclotron Facility, Bloomington, IN 47405.
d. National Laboratory for High Energy Physics, 1-1 Oho, Tsukuba, Ibaraki 305, Japan.
e. Physics Department, Hope College, Holland, MI 49423.
f. Brookhaven National Laboratory, Upton, NY 11973.

References

1. J. W. Harris *et al.*, Nucl. Phys. A **471**, 241c (1987); C. A. Ogilvie *et al.*, Phys. Rev. Lett. **67**, 1214 (1991); J. P. Alard *et al.*, Phys. Rev. Lett. **69**, 889 (1992).

2. Y. D. Kim *et al.*, Phys. Rev. Lett. **63**, 494 (1989); Y. Blumenfeld *et al.*, Phys. Rev. Lett. **66**, 576 (1991); E. Piasecki *et al.*, Phys. Rev. Lett. **66**, 1291 (1991); D. R. Bowman *et al.*, Phys. Rev. Lett. **67**, 1527 (1991); R. T. de Souza *et al.*, Phys. Lett. B **268**, 6 (1991); K. K. Hagel *et al.*, Phys. Rev. Lett. **68**, 2141 (1992); B. Lott *et al.*, Phys. Rev. Lett. **68**, 3141 (1992); T. C. Sangster *et al.*, Phys. Rev. C **46**, 1404 (1992); D. R. Bowman *et al.*, Phys. Rev. C **46**, 1834 (1992).

3. J. Bondorf, R. Donangelo, I. Mishustin, and H. Schulz, Nucl. Phys. A **444**, 460 (1985); D. Gross, Z. Xiao-ze, and X. Shu-yan, Phys. Rev. Lett. **56**, 1544 (1986).

4. W. A. Friedman and W. G. Lynch, Phys. Rev. C **28**, 16 (1983); W. A. Friedman, Phys. Rev. Lett. **60**, 2125 (1988).

5. Y. D. Kim *et al.*, Phys. Rev. C **45**, 387 (1992).

6. Y. D. Kim *et al.*, Phys. Rev. Lett. **67**, 14 (1991).

7. D. Fox *et al.*, Phys. Rev. C **47**, R421 (1993).

8. E. Bauge *et al.*, Phys. Rev. Lett. **70**, 3705 (1993).

9. T. C. Sangster *et al.*, Phys. Rev. C **47**, R2457 (1993).

10. D. R. Bowman *et al.*, Phys. Rev. Lett. **70**, 3534 (1993).

11. T. Ethvignot *et al.*, Phys. Rev. C **48**, 618 (1993); B. Kaempfer *et al.*, Phys. Rev. C **48**, R955 (1993).

12. L. Phair *et al.*, Nucl. Phys. A **548**, 489 (1992).

13. T. Glasmacher *et al.*, preprint MSUCL-923

EVENT SHAPE ANALYSIS OF ^{40}Ar + ^{232}Th AT E/A = 15 - 115 MeV

E.E. Gualtieri, J. Yee, D. Craig, S.A. Hannuschke, R. Lacey[a], T. Li, W.J. Llope, A. Nadasen[b], E. Norbeck[c], R. Pak, N.T.B. Stone, A. Vander Molen, G. D. Westfall, and S.J. Yennello[d]

Previous studies of Ar + Th reactions have given evidence that the process of fusion-fission, which dominates in central collisions at beam energies $\lesssim$20 MeV/nucleon, disappears as the beam energy is increased [1], and it has been speculated that multifragmentation becomes the dominant process. In order to learn more about these reaction mechanisms and possible transitions between them, we have studied Ar + Th reactions systematically versus beam energy from 15 to 115 MeV/nucleon. We have selected events based on two criteria: total transverse kinetic energy and the opening angle between very heavy fragments produced in the reactions. An event shape analysis was also used to characterize these events, and to search for trends which might indicate beam energy dependent changes in the dominant reaction mechanism.

The data was taken using the MSU 4π Array [2] and beams from the K1200 cyclotron. For this experiment the 4π Array was equipped with Multi-Wire Proportional Counters (MWPCs) [3] that provided position information about massive fragments (Z$\gtrsim$20), including fission fragments. Complete charge and energy identification for 1$\leq$Z$\leq$20 is provided by the phoswich and Bragg Curve counters (BCCs) in the Array. Figure 1 shows a typical position spectrum from the MWPCs in impact parameter inclusive events. In this spectrum, outlines of individual MWPC modules are visible, as is the shadowing from the target frame at approximately 90°.
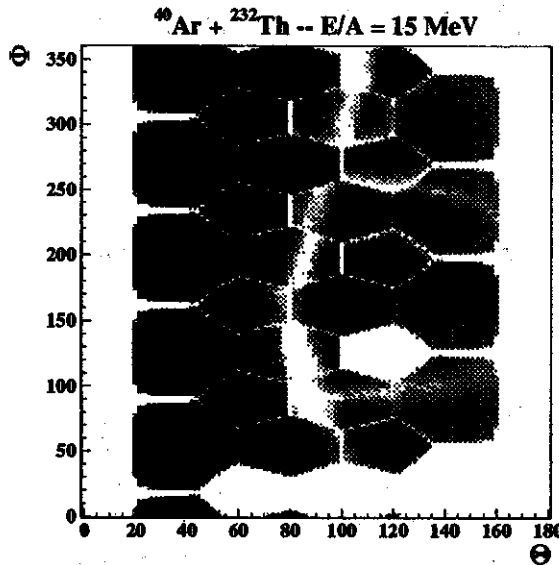

Figure 1: Example of an MWPC position spectrum

The opening angle between a pair of MWPC hits (labelled A and B) was defined via:

$$\cos\Theta_{AB} = \cos\theta_A \cos\theta_B + \sin\theta_A \sin\theta_B \cos(\phi_A - \phi_B)$$

Probability distributions of the opening angles are shown in Figure 2. Only events in which two or more MWPCs fired are shown. If more than two MWPCs fired in an event, the pair with the largest signal

pulseheights were used to calculate the opening angle. In this figure, two large peaks are generally visible. The first peak occurs at opening angles $\gtrsim 150°$, and is populated mainly by low momentum-transfer collisions followed by the fission of the Th target. The second peak occurs at smaller opening angles ($\sim 120°$ for the 15 MeV/nucleon case and $\sim 90°$ for 115 MeV/nucleon), and is populated mainly by high momentum-transfer collisions (e.g. fusion-fission or multifragmentation). The shaded areas indicate software gates on the two peaks that were used to select events in subsequent analyses described below.
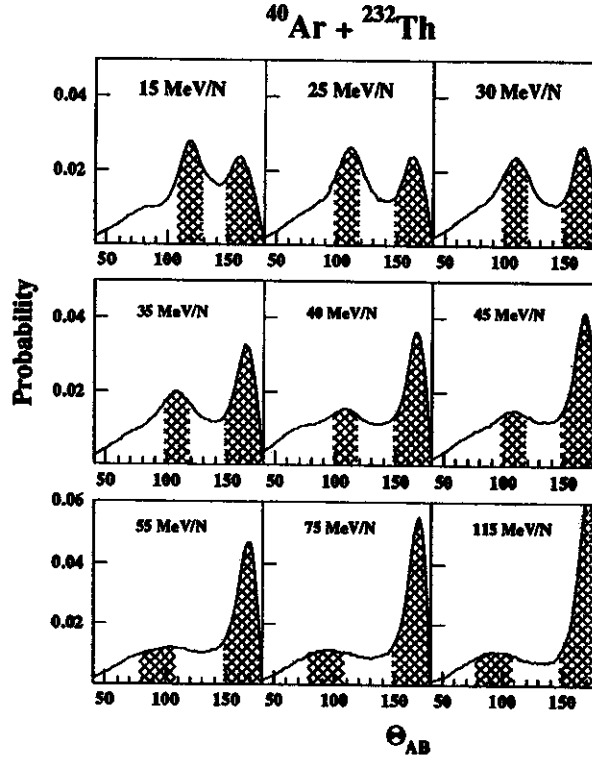
$$^{40}Ar + \,^{232}Th$$

Figure 2: Impact parameter inclusive probability distribution of opening angle in the lab frame. Shaded areas indicate software gates.

The impact parameter was constrained additionally using cuts on the total nonrelativistic transverse kinetic energy, which is defined as:

$$KE_t = \Sigma_i^{N_{id}} KE_i \sin^2 \theta_i$$

where the sum runs over only fully identified particles (N_{id}). KE_i is the laboratory particle kinetic energy and θ_i is its laboratory polar angle. Events with a total KE_t that fell in the top 10% of the inclusive KE_t distribution were assumed to be a "central" events (b $\lesssim 0.3(R_p + R_t)$). Events with a total $KE_t \leq 1\%$ of the projectile energy were assumed to be "peripheral" (b $\gtrsim 0.6(R_p + R_t)$).

Sphericity was used to indicate the average "shape" of the event in momentum space, and is constructed using the eigenvalues obtained from the kinetic flow tensor [4]. Only the fully identified particles from the phoswiches and BCCs were used to fill this tensor. It is expected that multifragmentation events will tend to have larger Sphericities than fusion-fission events. In fusion-fission events, particles are emitted preferentially along one axis due to the sequential binary nature of the decay, and so the event appears elongated, or rod-like, in momentum space. In multifragmentation events, where the breakup immediately produces many intermediate mass fragments, the particles are emitted more isotropically. Thus these events have a more spherical shape in momentum space, and accordingly, a higher Sphericity.

36

Figures 3a and 3b display the mean Sphericity, $<S>$, versus the projectile energy. Sphericity is averaged only over events with the same multiplicity (N_{id}), because this variable has a strong multiplicity dependence. In Figure 3a only events in the high-momentum transfer gate on the opening angles (c.f. Fig. 2) and the central KE_t gate are shown. In this subset of events, for the higher multiplicities, $<S>$ rises and falls as projectile energy increases and goes through a maximum at $\sim$55 - 60 MeV/nucleon. This a preliminary indication of a change in the dominant reaction mechanism. The lower multiplicities show a steady decline in $<S>$ with increasing beam energy. However, in this case the exclusion of the heavy fragments from the event shape calculation most likely affects the Sphericity significantly at the lower projectile energies.

In Figure 3b, only events in the low-momentum transfer gate that were also categorized as peripheral, using KE_t, are shown. The most striking feature in this plot, in comparison with Figure 3a, is the extremely suppressed value of $<S>$ for all multiplicities and energies. This because the shape of an event resulting from a peripheral collision is extremely elongated, even moreso than a central, sequential binary event. Also, if one notes the scale of the axes in 3b, one can see that the relative change in $<S>$ as projectile energy increases is minimal as compared to that of 3a. This is understandable because in peripheral collisions the excitation energy, and thus the reaction mechanism, is not expected to change significantly with beam energy.
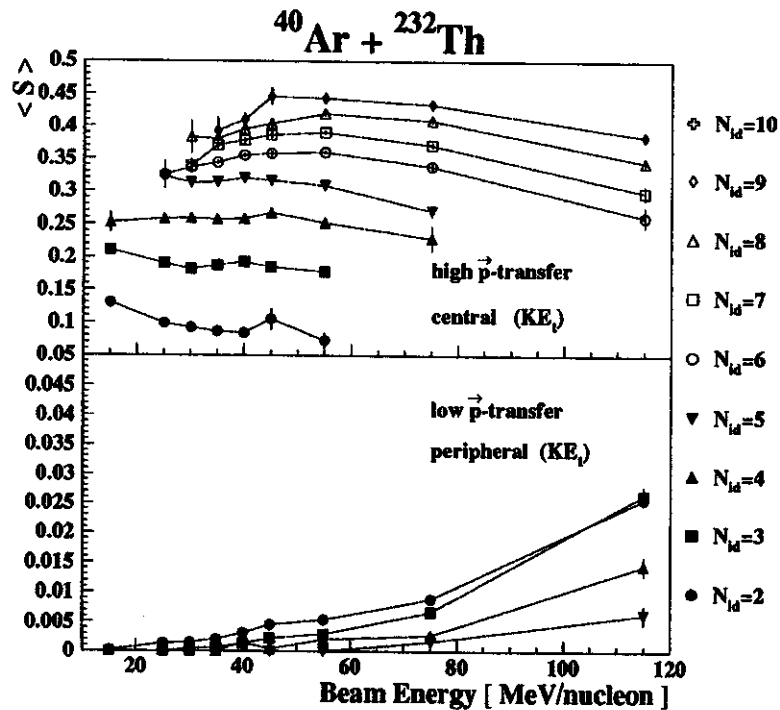

Figure 3: Mean Sphericity versus beam energy. Symbols indicate identified particle multiplicity(N_{id}).

We have seen that an opening angle and event shape analyses of Ar + Th collisions give an indication of a possible transition in the dominant reaction mechanism in central collisions at approximately 55-60 MeV/nucleon, and that there is no such indication if one looks at peripheral collisions. Future work will include the incorporation of the heaviest fragments into the shape analysis, and the study of other projections of the flow tensor.

a. Department of Chemistry, State University of New York at Stony Brook, Stony Brook NY 11794-3400
b. Department of Physics, University of Michigan at Dearborn, Dearborn, MI 48128
c. Department of Physics and Astronomy, University of Iowa, Iowa City, Iowa 52242
d. Department of Chemistry, Texas A&M University, College Station TX 77843

References

1. M. Conjeaud et. al.,Phys. Lett. **B159**, 244 (1985).
2. G.D. Westfall et. al., Nucl. Instr. and Meth. **A238**, (1985) 347.
3. J. Yee et. al.,Annual Report NSCL/MSU (1991).
4. M. Gyulassy et. al. Phys. Lett. **B110**, 185 (1982).

TRANSITIONS IN NUCLEAR DISASSEMBLY AS VIEWED BY FRAGMENT CHARGE CORRELATIONS

N. T. B. Stone, W. J. Llope, and G. D. Westfall

Particular trends in the slopes and functional form of the charge distributions of fragments emitted following central heavy-ion collisions have been noted [1,2,3] as strong signals for liquid-gas phase transitions in excited nuclei [1,4]. A relatively shallow power-law charge distribution for charges $1 \leq Z \lesssim 20$ is expected at the transitional excitation energy, as compared to steeper exponential distributions at energies both above and below. However, a power-law behavior of the fragment charge distributions may also result from averaging over impact parameters or excitation energies [2,5], imitating the expected signal of a liquid-gas phase transition. In this article, we propose observables based on the relative sizes of the three largest fragments following a systematic study of central $^{20}\text{Ne}+^{27}\text{Al}$, $^{40}\text{Ar}+^{45}\text{Sc}$, $^{84}\text{Kr}+^{93}\text{Nb}$, and $^{129}\text{Xe}+^{139}\text{La}$ reactions. These observables, D_{cent} and D_{edge}, are extracted from charge Dalitz plots [6], and used to evaluate the importance of sequential binary (SB) [7,8,9,10,11] and multifragmentation (MF) [11,12] disassembly mechanisms in the small impact parameter events. The observation of a transition from SB disassembly to MF for increasing beam energies would be suggestive of the transition from liquid to liquid-gas coexistence phases, i.e. the "cracking" transition, that has been predicted by several models [12,13].

Each central event is assigned a location in an equilateral triangle of unit altitude by equating the distances to the three sides of the triangle to the relative charges of the three largest fragments, i.e. $Z_i' = Z_i/Z_{sum}$, where $Z_1(Z_3)$ is the charge of the largest(third largest) fragment and $Z_{sum} = \sum_{i=1}^{3} Z_i$. We define the distance from each entry to the geometric center of the triangle, $D_{cent} = \sqrt{(Z_1' \tan 30° + Z_2'/\cos 30° - \frac{1}{\sqrt{3}})^2 + (Z_1' - \frac{1}{3})^2}$, and the perpendicular distance to the nearest edge, $D_{edge} = Z_3'$. Events with three or more nearly equally sized largest fragments will populate the center of the triangle ($D_{cent} < D_{edge}$), while those with one large fragment and two smaller, or two large fragments and one smaller, will populate the corners or sides of the triangle, respectively ($D_{cent} > D_{edge}$). These possibilities can be assumed to be populated predominantly by specific nuclear disassembly mechanisms [6].

We classify as sequential binary those disassembly mechanisms involving a cascade of two-body decay steps, in which each step is independent and may involve (a)symmetric binary fission [7,8], (a)symmetric ternary fission [9], or evaporation [7,10]. Over the course of a purely evaporative SB decay, the probability of emitting large fragments decreases due to the increasing importance of the Coulomb and angular momentum barriers. The three largest charges in final states produced in such SB decays would thus be expected to consist of one larger fragment and two smaller ones. A binary or ternary fission step in the SB decay cascade would result in the emission of two larger fragments and one smaller one. Disassembly leading to three similarly sized largest fragments has been noted as a signal for the process known as multifragmentation [11,12]. For some sample of events, we therefore make the assignment that $\langle D_{cent} \rangle > \langle D_{edge} \rangle$ implies the predominance of SB disassembly, while $\langle D_{cent} \rangle < \langle D_{edge} \rangle$ implies multifragmentation. In the central events with $\langle D_{cent} \rangle > \langle D_{edge} \rangle$, a population near the corners of the charge Dalitz triangles implies asymmetric fission or sequential evaporative decays, while one near the sides implies symmetric binary or ternary fission [6].

The reactions studied were $^{20}\text{Ne}+^{27}\text{Al}$ at beam energies of 55, 75, 95, 105, 115, 125, 135, and 140

MeV/nucleon; ^{40}Ar+^{45}Sc at 15, 25, 35, 45, 65, 75, 85, 95, 105, and 115 MeV/nucleon; ^{84}Kr+^{93}Nb at 35, 45, 55, 65, and 75 MeV/nucleon; and ^{129}Xe+^{139}La at 25, 30, 35, 40, 45, 50, 55, and 60 MeV/nucleon. The beams were obtained from the K1200 cyclotron at the National Superconducting Cyclotron Laboratory, and all of the data were collected using the MSU 4π Array [14] with a minimum bias trigger (two discriminator hits). The fragment charges were well resolved over the range $1 \leq Z \leq 15$ in the ^{20}Ne+^{27}Al and ^{84}Kr+^{93}Nb entrance channels, and $1 \leq Z \leq 18$ in the ^{40}Ar+^{45}Sc and ^{129}Xe+^{139}La entrance channels. Further information concerning the apparatus and data collection can be found in Refs. [14,15]. The distortions to the present results that are caused by the inefficiencies in experimental measurement were studied using events generated by model codes and a software replica of the detection system. These are discussed as appropriate below.

The total mass and excitation energy of the excited systems formed for each reaction are constrained via the selection of the most central collisions. Separate impact parameter cuts allowing the $\sim$10% most central of the minimum bias events were placed on a number of different variables. These include the total number of charged particles measured in an event (N_c), the total number of protons (N_p), the total charge in hydrogen and helium fragments (Z_{lcp}), the total transverse kinetic energy (KE_T), and the total charge of all particles in a software gate centered at mid-rapidity (Z_{MR}). The variables KE_T and Z_{MR} are defined as in Ref. [16]. Autocorrelations between the present relative charge observables and each of these centrality variables were investigated via the comparison of the widths of these observables in the events selected by the $\sim$10% cuts on each of these centrality variables separately. Such autocorrelations result in a significant suppression of these widths, as compared to those resulting from cuts on non-autocorrelating centrality variables. The widths of the distributions of Z_1, Z_2, and Z_3 resulting from cuts on N_c, N_p, and Z_{lcp} were found to be suppressed by as much as a factor of two relative to the corresponding distributions following small impact parameter cuts on the variables KE_T and Z_{MR}. The widths of the D_{cent} and D_{edge} distributions were also suppressed following cuts on these three variables. Therefore, the centrality variables N_c, N_p, and Z_{lcp}, are significantly autocorrelated with the present relative charge observables. Two-dimensional small impact parameter cuts based on the variables KE_T and Z_{MR} will therefore be employed, which allow the 4-8% most central of the minimum bias events. According to approximate geometrical arguments, these events have average impact parameters $\langle b \rangle \lesssim 0.25 b_{max}$, where b_{max} is roughly the sum of the radii of the projectile and target nuclei.

It is noted, however, that there are hidden constraints in this charge correlation analysis. For example, events characterized by a low value of Z_{sum} cannot, by definition, populate the extreme corners or sides of the Dalitz triangles. Indeed, there are well-defined maximum and minimum possible values of D_{cent} and D_{edge} for each value of Z_{sum}. These extrema are shown for D_{edge} in Figure 1 as the solid lines (analogous limits apply for D_{cent}). As Z_{sum} is decreased, the range of possible values of D_{edge} decreases, and this range tends towards larger values of D_{edge}. It is therefore possible that changes in the values of these observables may simply reflect similarly beam energy dependent decreases in the average values of Z_{sum}. The values of Z_{sum} averaged over beam energies in each entrance channel are 6.7, 9.9, 15.7, and 19.0, for the ^{20}Ne+^{27}Al through ^{129}Xe+^{139}La systems, which correspond to 29%, 25%, 20%, and 17% of the total entrance channel charge. The percentage standard deviations about these average values over the different beam energies in each entrance channel are 8%, 12%, 3%, and 7%. Thus, $\langle Z_{sum} \rangle$ is only weakly dependent on the beam energy in each entrance channel, so that this effect can be neglected. The average values of D_{edge} are also plotted in this Figure for three representative beam energies in each entrance channel. These reveal a dependence of D_{edge} (and D_{cent}) on Z_{sum} that generally follows the shape of the
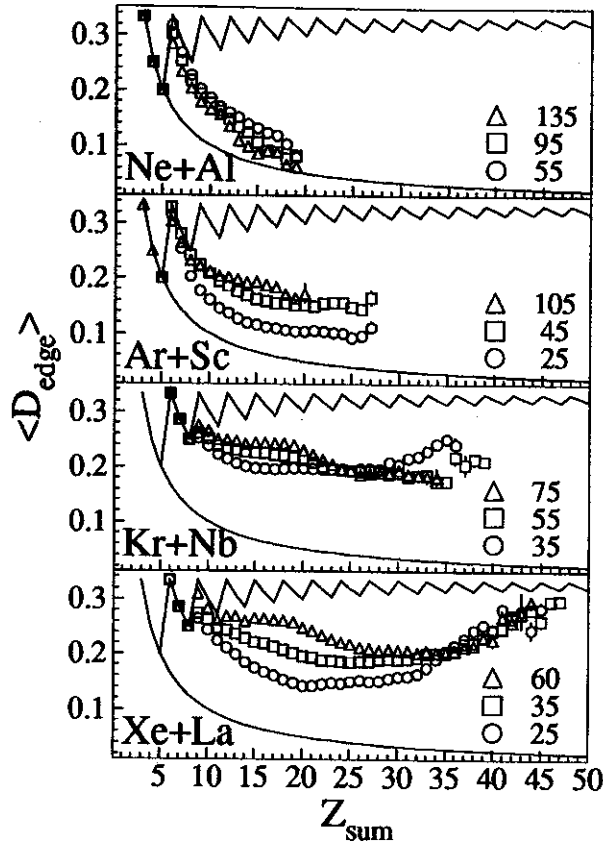
Figure 1: The average values of D_{edge} versus Z_{sum} in the central events for three representative beam energies in MeV/nucleon for each entrance channel, as labeled. The solid lines indicate the minimum and maximum values of D_{edge} that are possible for each value of Z_{sum} by definition.

region allowed by definition. For $3 \leq Z_{sum} \leq 5$, there is only one allowed value of D_{edge} (and D_{cent}). While no relative charge information can be extracted for $3 \leq Z_{sum} \leq 5$, central events with relatively small values of Z_{sum} are nonetheless interesting. These indicate events in which no large fragments were observed, implying the rather complete vaporization of the system.

It is also important to consider also the constraints on the present observables that are imposed by the inefficiencies of the detection system. The most obvious constraint of this kind results from the maximum charge that could be detected, which was ~ 15 for the ^{20}Ne+^{27}Al and ^{87}Kr+^{93}Nb reactions, and ~ 18 for the ^{40}Ar+^{45}Sc and ^{129}Xe+^{139}La reactions. The effect of this limit is to decrease the sensitivity of the present observables for large values of Z_{sum}. Specifically, as the values of Z_1 and Z_2 approach the maximum detectable charge, the number of possible permutations of Z_1, Z_2, and Z_3 having the same measured Z_{sum} decreases. This leads to a situation similar to that for $3 \leq Z_{sum} \leq 5$, where the limited range of possible values for D_{cent} and D_{edge} reduces their sensitivity. In Figure 1, the values of $\langle D_{edge} \rangle$ manifest fairly abrupt changes at roughly the maximum detected charge plus two, and twice that maximum plus one, corresponding to the detection of such maximum charges in coincidence with protons.

The average values of D_{cent} (with points) and D_{edge} (without points) are depicted in Figure 2 for those central events with $6 \leq Z_{sum} \leq 17$, for the ^{20}Ne+^{27}Al and ^{87}Kr+^{93}Nb entrance channels, and $6 \leq Z_{sum} \leq 20$, for the ^{40}Ar+^{45}Sc and ^{129}Xe+^{139}La entrance channels. For the lowest beam energies in both the ^{40}Ar+^{45}Sc and ^{129}Xe+^{139}La systems, $\langle D_{cent} \rangle > \langle D_{edge} \rangle$ for central events. This implies an overall
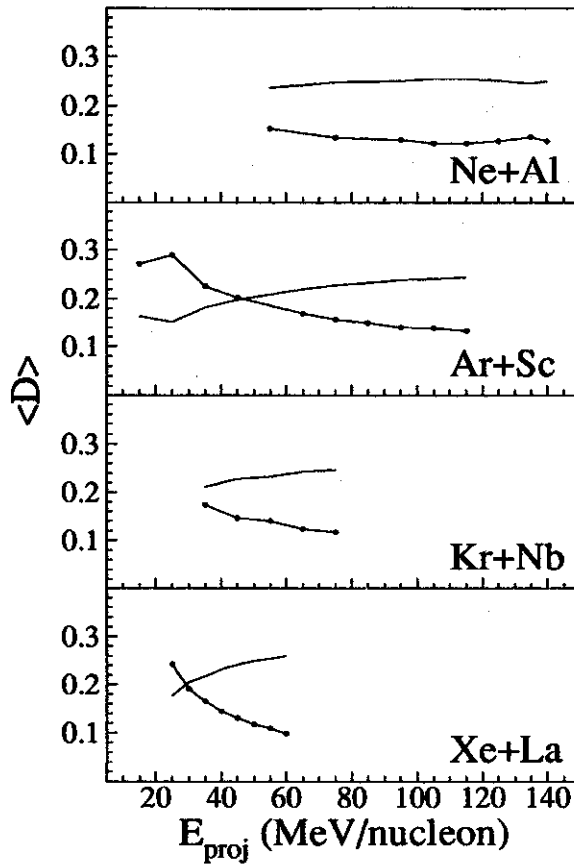
Figure 2: The average values of D_{cent} (with points) and D_{edge} (without points) versus the beam energy for specific gates on the quantity Z_{sum}: $6 \leq Z_{sum} \leq 17$ for the ^{20}Ne+^{27}Al and ^{87}Kr+^{93}Nb entrance channels, and $6 \leq Z_{sum} \leq 20$ for the ^{40}Ar+^{45}Sc and ^{129}Xe+^{139}La entrance channels.

asymmetry in the charges of the largest three fragments in these events, and is thus consistent with a SB disassembly mechanism. These events predominantly populate the corners of the charge Dalitz triangles, implying that asymmetric fission or sequential evaporation decays are more common than those involving a symmetric binary or ternary fission. For higher beam energies in these entrance channels, as well as for all of the beam energies in the ^{20}Ne+^{27}Al and ^{87}Kr+^{93}Nb entrance channels, $\langle D_{cent} \rangle < \langle D_{edge} \rangle$. The largest three fragments in these final states are thus similarly sized, implying multifragmentation.

A beam energy that is transitional between SB and MF disassembly is defined at the crossing of the lines interpolated from the points shown in Figure 2. The transitional beam energies extracted for the central ^{40}Ar+^{45}Sc and ^{129}Xe+^{139}La reactions are 47±5 and 29±5 MeV/nucleon, respectively. The results for the central ^{87}Kr+^{93}Nb reactions are similar to those for the central ^{129}Xe+^{139}La reactions, implying a transitional beam energy somewhere in the range of 30-35 MeV/nucleon for this system. The average distances in the central ^{20}Ne+^{27}Al reactions are generally consistent with those observed in the ^{40}Ar+^{45}Sc reactions at the same beam energies. The values of $\langle D_{cent} \rangle$ and $\langle D_{edge} \rangle$ appear to reach asymptotic values within a few tens of MeV/nucleon above the transitional beam energies.

A more complete investigation of the effects of the experimental acceptance involves the generation of software events, and the comparison of the present relative charge observables in these events with and without filtering by a software replica of the apparatus. The filter code includes a complete description of the geometry and the kinetic energy thresholds. Multiple hits in individual detector elements are treated

in consistency with the templates used to calibrate all of the experimental data. Separate samples of events were generated with the Berlin code [17], each at a specified excitation energy, in a system expected to be common in the present central ^{40}Ar+^{45}Sc reactions ($Z{\sim}31$, $A{\sim}68$). The upper two frames in Figure 3 depict $\langle Z_{sum} \rangle$ and $\langle D_{cent} \rangle$ after each of these samples of events is boosted from the center of momentum
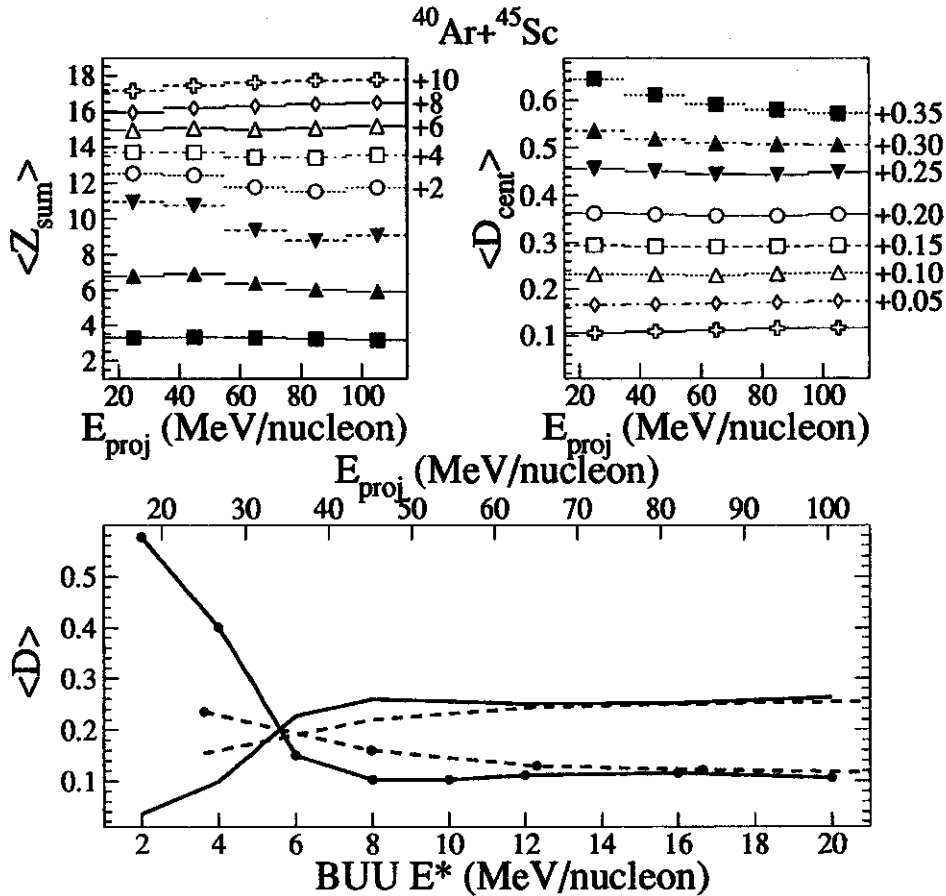

Figure 3: The average values of Z_{sum} (upper left frame) and D_{cent} (upper right frame) obtained from eight samples of events, each generated at a specific excitation energy for central ^{40}Ar+^{45}Sc reactions using the Berlin code. Each sample is boosted from the CM frame to the laboratory, and then filtered, for beam energies from 25 to 105 MeV/nucleon. Some points in the upper frames have been offset for clarity by the amounts shown to the right. The lower frame compares the excitation energy dependence of the unfiltered Berlin events with the beam energy dependence of the filtered Berlin events, using BUU calculations to relate the beam and excitation energies for central ^{40}Ar+^{45}Sc reactions.

frame into the laboratory, and then filtered, for beam energies in the range of 25 to 105 MeV/nucleon. The events were generated at excitation energies of 2 (solid squares), 4, 6, 8, 10, 12, 16, and 20 (open crosses) MeV/nucleon. The filtered $\langle Z_{sum} \rangle$ and $\langle D_{cent} \rangle$ show only a very weak dependence on the magnitude of the boost into the laboratory for all of the samples of generated events. The crossings noted in Figure 2 are therefore not the result of a strong beam energy dependence of the experimental acceptance.

The solid curves in the lower frame in Figure 3 depict the excitation energy dependence of $\langle D_{cent} \rangle$ (with points) and $\langle D_{edge} \rangle$ (without points) for the unfiltered Berlin events. The unfiltered Berlin events evolve from the corners to the center of the charge Dalitz triangles, and exhibit a crossing excitation energy near 6 MeV/nucleon. Boltzmann-Uehling-Uehlenbeck (BUU) calculations are one means of specifying the

relationship between the beam energy and the average excitation energy for central collisions. These calculations were performed as described in Ref. [18], and the predicted relationship between the beam and excitation energies is visible by comparing the upper and lower abscissa in this lower frame. The dotted lines in this frame depict the values of $\langle D_{cent} \rangle$ and $\langle D_{edge} \rangle$ following the boosting and filtering of the generated events assuming this relationship. The apparent crossing (beam) energy is only weakly affected by the imposition of the experimental inefficiencies via the software filter. The major effect is to reduce the apparent asymmetry of the three largest charges for asymmetric events, i.e. those in the SB region.

This article has described a method of evaluating the importance of the specific disassembly mechanisms in a comprehensive set of central heavy-ion reactions using charge Dalitz plots. Small impact parameter collisions were selected using two-dimensional cuts on centrality variables that do not autocorrelate with the relative charge distributions. The observables D_{cent} and D_{edge} were introduced for the purpose of quantifying the distribution of events in the charge Dalitz triangles for each reaction. The constraints imposed on these observables, by definition and by the inefficiencies in the detection system, were shown not to affect our conclusions. Transitions from sequential binary disassembly to multifragmentation were observed in the central ^{40}Ar+^{45}Sc and ^{129}Xe+^{139}La entrance channels at beam energies of ~47 and ~29 MeV/nucleon, respectively. The results for the central ^{20}Ne+^{27}Al (^{84}Kr+^{93}Nb) reactions are consistent with the trends noted for the central ^{40}Ar+^{45}Sc(^{129}Xe+^{139}La) reactions over a more limited range of available beam energies.

References

1. M.E. Fisher, Physics (Long Island City, NY) 3, 255 (1967).
2. W. Bauer, Phys. Rev. C 38, 1297 (1988), and references therein.
3. X. Campi, Phys. Lett. B208, 351 (1988); D. Stauffer, Phys. Rep. 54, 1 (1979); A.S. Hirsch *et al.*, Phys. Rev. C 29, 508 (1984); J.E. Finn *et al.*, Phys. Rev. Lett. 49, 1321 (1982).
4. A.L. Goodman, J.I. Kapusta, and A.Z. Mekjian, Phys. Rev. C 30, 851 (1984); A.D. Panagiotou *et al.*, Phys. Rev. Lett. 52, 496 (1984).
5. J. Aichelin *et al.*, Phys. Rev. C 37, 2451 (1988); T. Li *et al.*, Phys. Rev. Lett. 70, 1924 (1993).
6. P. Kreutz *et al.*, Nucl. Phys. A556, 672 (1993); P. Roussel-Chomaz *et al.*, Nuc. Phys. A551, 508 (1993); G. Bizard *et al.*, Phys. Lett. B302, 162 (1993); M. Colonna *et al.*, Phys. Lett. B283, 180 (1992).
7. C. Barbagallo, J. Richert, and P. Wagner, Z. Phys. A 324, 97 (1986); R.J. Charity *et al.*, Nucl. Phys. A483, 371 (1988).
8. G. Casini *et al.*, Phys. Rev. Lett. 71, 2567 (1993); H. Delagrange *et al.*, Z. Phys. A. 323, 437 (1986).
9. K. Siwek-Wilczynska *et al.*, Phys. Rev. C 48, 228 (1993); M. Sowiński *et al.*, Z. Phys. A. 324, 87 (1986).
10. F. Pühlhofer, Nucl. Phys. A280, 267 (1977).
11. L.G. Moretto and G.J. Wozniak, Ann. Rev. Nucl. Part. Sci. (May, 1993).
12. J.P. Bondorf *et al.*, Nucl. Phys. A448, 753 (1986), and references therein; A.S. Botvina *et al.*, Nucl. Phys. A475, 663 (1987); D.H.E. Gross, Proj. Part. Nucl. Phys. 30, 155 (1993), and references therein.
13. D.H.E. Gross and H. Massmann, Nucl. Phys. A471, 339c (1987).
14. G.D. Westfall *et al.*, Nuc. Inst. and Meth. A238, 347 (1985).
15. G.D. Westfall *et al.*, Phys. Rev. Lett. 71, 1986 (1993).
16. L. Phair *et al.*, Nucl. Phys. A548, 489 (1992).
17. X.-Z. Zhang *et al.*, Nucl. Phys. A461, 668 (1987), and references therein.
18. C.M. Mader, Ph.D. Thesis, Michigan State University, 1993 (unpublished); D.R. Bowman *et al.*, Phys. Rev. C 46, 1834 (1992).

AUTOCORRELATIONS IN THE SELECTION OF SMALL IMPACT PARAMETER HEAVY-ION COLLISIONS.

W.J. Llope, J.A. Conrad[a], D. Craig, E. Gualtieri, S. Hannuschke, R.A. Lacey[b],
J. Lauret[b], T. Li, A. Nadasen[c], E. Norbeck[d], R. Pak, N.T.B. Stone,
A.M. Vander Molen, G.D. Westfall, J. Yee, and S.J. Yennello[e].

Perhaps the most direct study of multifragment final states following intermediate energy heavy-ion collisions involves the experimental measurement of the average number of intermediate mass fragments (IMFs, for which $3 \leq Z \lesssim 20$) emitted in such reactions. A number of physical processes governing the disassembly of excited nuclei can result in the emission of such fragments (see the recent review by Moretto and Wozniak [1]), and many model code event generators embodying these processes are available. One general class of these models is fundamentally "sequential binary", i.e. these describe the disassembly as a series of two-body decay steps, each involving (a)symmetric fission or statistical evaporation. An alternative description is provided by several similar "multifragmentation" models, which assume chemical and thermal equilibrium has been obtained in an expanded spherical freeze-out volume of prescribed size. Previously reported comparisons of the results obtained from models in these two general classes imply that larger multiplicities of IMFs are obtained from the multifragmentation models, as compared to the sequential binary models run with the same set of input parameters [2]. This observation was, however, subsequently contested [3]. Systematic experimental measurements of IMF emission from nuclear systems covering a wide range of mass and excitation are required, allowing the confrontation of all the various theoretical predictions with experimental results.

The experimental data were collected with the Michigan State University 4π Array [4] at the National Superconducting Cyclotron Laboratory (NSCL) using beams extracted from the K1200 cyclotron. Four symmetric entrance channels were systematically studied over a wide range of intermediate beam energies. The reactions include ^{20}Ne+^{27}Al at 55, 75, 95, 105, 115, 125, 135 MeV/nucleon, ^{40}Ar+^{45}Sc at 15, 25, 35, 45, 65, 75, 85, 105, 115 MeV/nucleon, ^{84}Kr+^{93}Nb at 35, 45, 55, 65, 75 MeV/nucleon, and ^{129}Xe+^{139}La at 25, 35, 45, 50, 55, 60 MeV/nucleon. Detailed descriptions of the apparatus and the data collection can be found in Refs. [4, 5].

In central heavy-ion reactions there are large probabilities for the formation of highly excited nuclear systems that contain most of the nucleons in the entrance channel. The excitation energies in these systems are monotonic functions of the beam energy. Such events can be selected offline via software cuts on experimental variables that are correlated with the impact parameter. The variable upon which a centrality cut is made must be tightly correlated with the impact parameter, and negligibly correlated with the experimental observable in all ways except that via the impact parameter. A significant correlation between an experimental observable and the centrality variable (beyond that due to the impact parameter) can be caused by charge, mass, or momentum conservation laws. Such "autocorrelations" may artificially enhance or suppress the values of the experimental observable in the events selected by perfunctory centrality cuts.

There is an intrinsic width to experimental observables in perfectly central collisions that is caused by the stochastic nature of the evolution of the excited nuclear systems formed in these collisions. Additional experimental contributions to this width result from any dependence of the experimental acceptance on the orientation of these excited systems in the laboratory, and from any inefficiencies in

the selection of the most central collisions. These experimental contributions can be understood via the study of the effect that a software replica of the experimental apparatus has on events generated by model codes at specific impact parameters. In principle, the intrinsic width carries important physical information concerning fluctuations during the reactions. The measured width can, after the treatment of the experimental contributions, be defined as the intrinsic width, unless there are non-negligible autocorrelations between the observable O and the experimental variable used to select the central events.

It is assumed that the variance, $\sigma_O^2 = \langle O^2 \rangle - \langle O \rangle^2$, of an observable, O, in a sample of selected events is suppressed if a significant autocorrelation exists, and is equal to the intrinsic variance or width (modified by experimental considerations) otherwise. The importance of such autocorrelations during the use of a particular centrality variable can thus be inferred by the comparison of the variance of the observable following the selection of events using many different centrality variables. The cut(s) leading to the largest variances, σ_O^2, in the selected events are assumed to be the least autocorrelated with O. Two classes of autocorrelations between a centrality cut and an experimental observable can be defined based on the effects that such autocorrelations have on the normalized variance, $\sigma_O^2/\langle O \rangle$, in the selected events. Centrality cuts which result in a suppressed variance and a suppressed(enhanced) normalized variance will be referred to as positive(negative) autocorrelators, as they artificially enhance(suppress) $\langle O \rangle$.

The following variables are assumed to be correlated with the impact parameter: (i) the number of charged particles (N_{chgd}) detected in each event, (ii) the total charge detected in a software gate centered at mid-rapidity (Z_{MR}), (iii) the total transverse kinetic energy (KE_T), (iv) the number of detected hydrogen isotopes (N_H), (v) the total detected charge (Z_{det}), and (vi) the total charge of hydrogen and helium isotopes particles (Z_{LCP}). The variables Z_{MR} and KE_T are defined as in Ref. [6]. Separate samples of events are formed by placing thresholds on the impact parameter inclusive spectra of each of these variables which allow the most central ~10% of the events. For all of the centrality variables that are integer quantities, i.e. all but KE_T, it is not always possible to locate a threshold such that exactly 10% of the minimum bias events are selected. The threshold was thus defined for each centrality variable and reaction as the lowest bin for which $\leq$10% of the impact parameter inclusive events are in or above this bin. According to approximate geometrical arguments, thresholds allowing 10% of the impact parameter inclusive events allow average impact parameters $\langle b \rangle \sim 0.31b_{max}$. The quantity b_{max} is the largest impact parameter satisfying the minimum bias trigger used to collect these data, which required two or more charged particle hits in the MSU 4π Array. The quantity b_{max} is typically assumed to equal $[R_P + R_T]$, where $R_P(R_T)$ is the radius of the projectile(target) nucleus.

In Figure 1, the means (upper frames), variances (middle frames), and normalized variances (lower frames) of the N_{IMF} distributions are presented versus the beam energy in the six samples of selected small impact parameter events. The results for the ^{20}Ne+^{27}Al, ^{40}Ar+^{45}Sc, ^{84}Kr+^{93}Nb, and ^{129}Xe+^{139}La reactions are shown.

For all four entrance channels, the beam energy dependence of the IMF multiplicity observables is generally not affected by the particular choice of the variable used to select the small impact parameter events. In the ^{20}Ne+^{27}Al reactions ($E_{proj} \geq 55$ MeV/nucleon), the values of $\langle N_{IMF} \rangle$ decrease with increasing beam energies. In the ^{40}Ar+^{45}Sc reactions, the experimental values of $\langle N_{IMF} \rangle$ increase with increasing beam energies up to about 35 MeV/nucleon, and then fall off slowly for larger beam energies. For both of the heavier systems, ^{84}Kr+^{93}Nb ($E_{proj} \leq 75$ MeV/nucleon) and ^{129}Xe+^{139}La ($E_{proj} \leq 60$ MeV/nucleon), the values of $\langle N_{IMF} \rangle$ increase with increasing beam energies.

The IMF multiplicity observables in the events selected by the six different centrality cuts generally
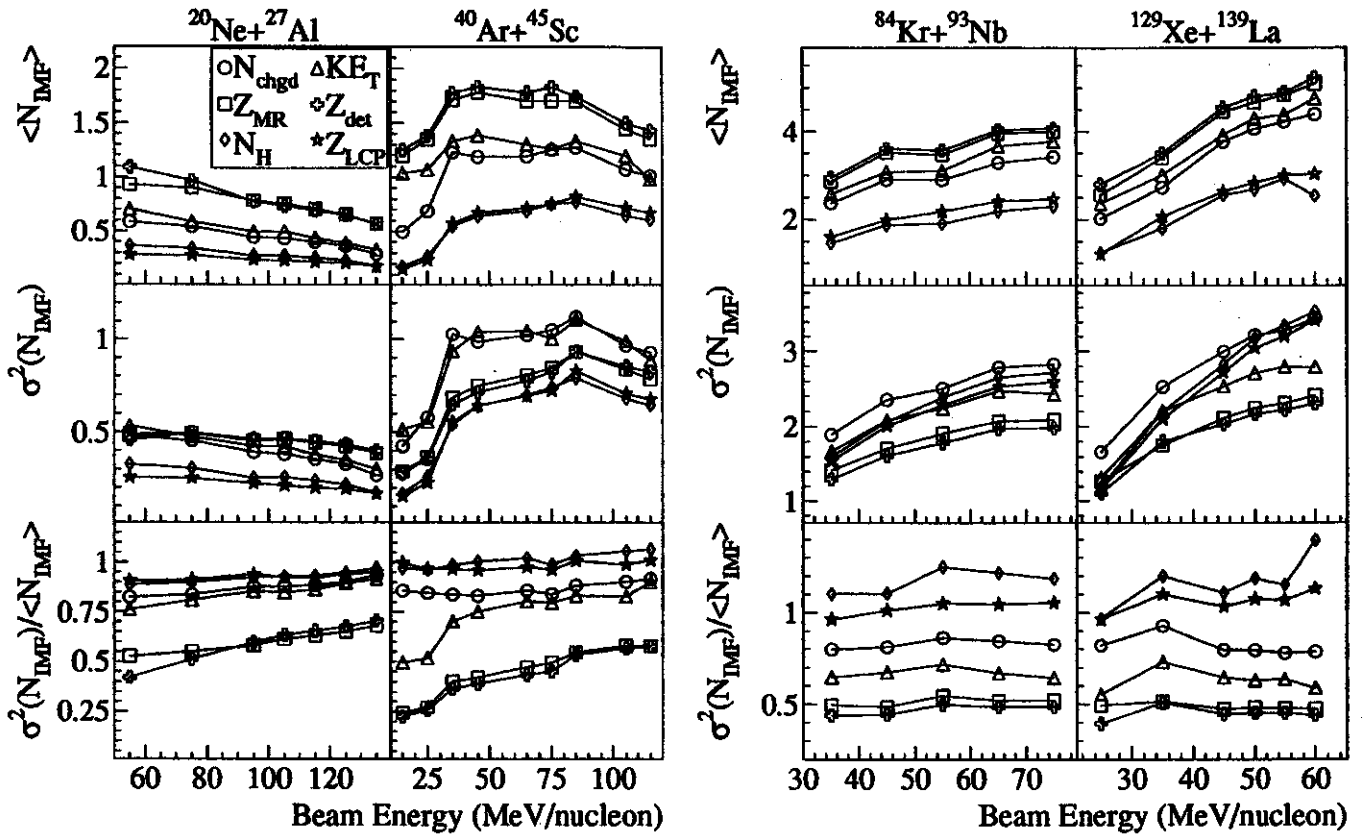
Figure 1: The means, variances, and normalized variances of the IMF multiplicities versus the beam energy in the six separate samples of small impact parameter events for the ^{20}Ne+^{27}Al, ^{40}Ar+^{45}Sc ^{84}Kr+^{93}Nb, and ^{129}Xe+^{139}La reactions.

form three distinct groups independent of the beam energy. Centrality cuts on the variables Z_{MR} and Z_{det} result in N_{IMF} distributions with relatively small variances and small normalized variances, while cuts on the variables N_H and Z_{LCP} result in relatively small variances and relatively large normalized variances. The events selected by the cuts on the variables N_{chgd} and KE_T have the relatively largest variances and intermediate normalized variances. Some exceptions to these trends in $\sigma^2(N_{IMF})$ are noted. At the highest beam energies in the ^{20}Ne+^{27}Al entrance channel, the variances following the Z_{MR} and Z_{det} cuts exceed those following the N_{chgd} and KE_T cuts. In the two heavier systems, the variances from the N_H and Z_{LCP} cuts are similar to those from the N_{chgd} and KE_T cuts (and relatively large). However, for all of the reactions, the normalized variances are always ordered in the same way.

The formation of these groups is generally independent of the beam energy and the entrance channel mass, which implies that the grouping is the consequence of an internal effect rather than physical one. The formation of these groups is a reflection of autocorrelations between some of these centrality variables and N_{IMF}. The centrality variables N_H and Z_{LCP} apparently suppress $\langle N_{IMF} \rangle$ (and σ^2) and are thus defined to be negative autocorrelators, while the variables Z_{MR} and Z_{det} artificially enhance $\langle N_{IMF} \rangle$ and are labelled positive autocorrelators. Given the dramatic distortions to IMF multiplicity observables seen in Figure 1 that result from centrality cuts on variables that autocorrelate with N_{IMF}, the only acceptable study of these observables in the central collisions in these data must involve cuts on N_{chgd} and/or KE_T. Figure 1 implies that the negative autocorrelation between the light particle multiplicity variables and N_{IMF} is somewhat stronger than the positive autocorrelation between N_{IMF}

47

and the variables Z_{MR} and Z_{det}.

To limit the selection of larger impact parameter events with significant topological fluctuations, a two-dimensional cut is placed on the centrality variables N_{chgd} and KE_T for all of the systems and beam energies. Only the events that fall above the thresholds located as described above (each allowing $\lesssim 10\%$ of the events) for both of these variables are selected. This results in the selection of $\sim$4-7% of the events, which have average impact parameters $\langle b \rangle \sim 0.20 - 0.26\, b_{max}$ geometrically.
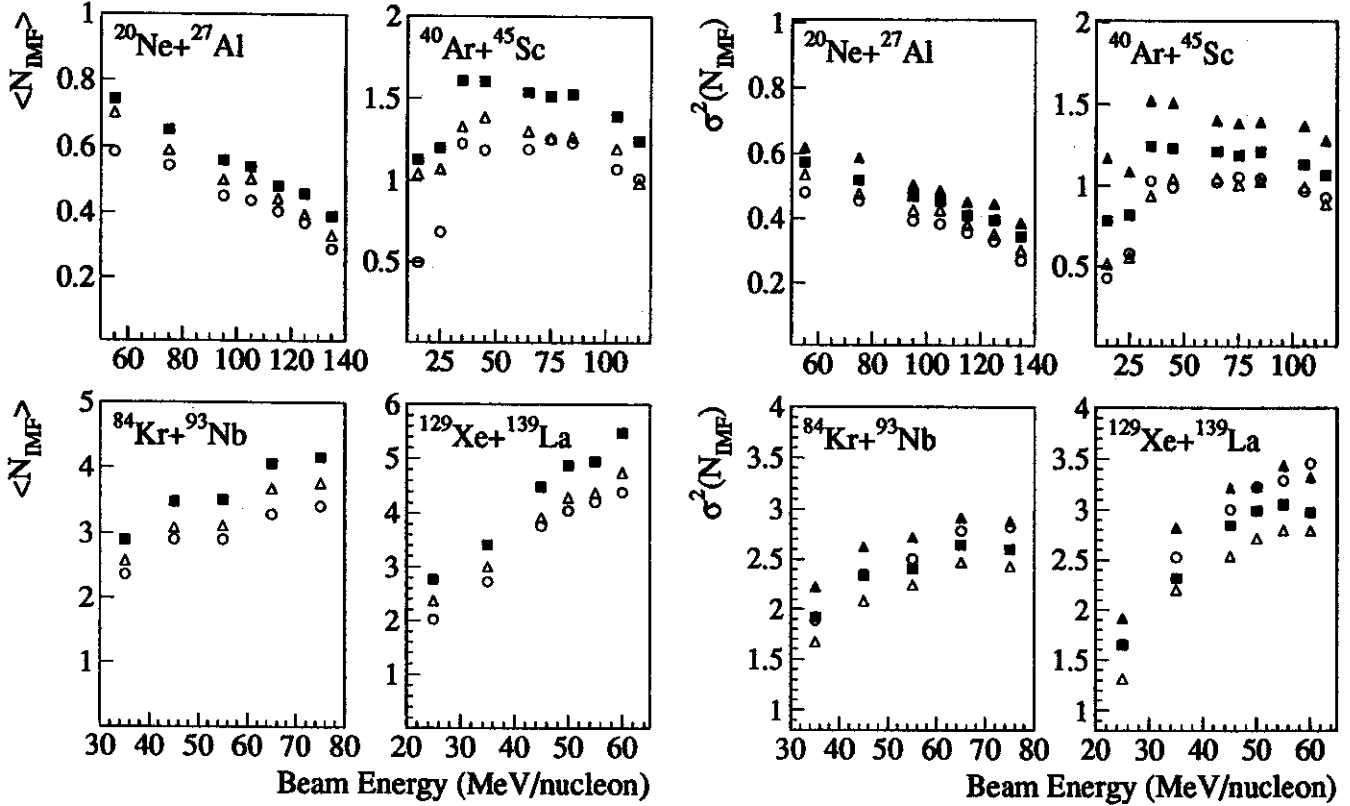

Figure 2: The average number of IMFs (left frames), and the N_{IMF} variances (right frames), versus the beam energy for three samples of small impact parameter events. Shown are the results following the two-dimensional $\sim$10% cuts on N_{chgd} and KE_T (solid squares), and following the two one-dimensional $\sim$10% cuts on N_{chgd} (open circles), and KE_T (open triangles). Also shown in the right frames are the N_{IMF} variances following two-dimensional $\sim$2% cuts on N_{chgd} and KE_T (solid triangles).

The mean multiplicities of IMFs in the events selected by these two-dimensional cuts are shown for all of the entrance channels and beam energies in Figure 2 as the solid squares. The average IMF multiplicities in the events selected by the two one-dimensional cuts on N_{chgd} (open circles) and KE_T (open triangles) are also shown. The events selected by the two-dimensional cut exhibit larger values of $\langle N_{IMF} \rangle$ as compared to those following either of the one-dimensional cuts. For increasing beam energies, the values of $\langle N_{IMF} \rangle$ decrease in the central ^{20}Ne+^{27}Al reactions ($E_{proj} \geq 55$ MeV/nucleon), rise then fall in the central ^{40}Ar+^{45}Sc reactions, and increase in the central ^{84}Kr+^{93}Nb ($E_{proj} \leq 75$ MeV/nucleon) and ^{129}Xe+^{139}La reactions ($E_{proj} \leq 60$ MeV/nucleon). The average IMF multiplicities range from $\sim$0.4 for the highest energy ^{20}Ne+^{27}Al reactions to $\sim$5.5 for the highest energy ^{129}Xe+^{139}La reactions

The variances, $\sigma^2(N_{IMF})$, in these same samples of small impact parameter events are also shown in Figure 2. The variances from the two-dimensional $\sim$10% cuts (solid squares) are larger than the

variances from the two one-dimensional cuts (open circles and triangles) in the ^{20}Ne+^{27}Al and ^{40}Ar+^{45}Sc reactions, and they are similar to or between the values from the two one-dimensional cuts in the ^{84}Kr+^{93}Nb and ^{129}Xe+^{139}La reactions.

Also included in this Figure are the N_{IMF} variances from stricter two-dimensional ~2% cuts on N_{chgd} and KE_T (solid triangles). It is important to note that the N_{IMF} variances from these stricter two-dimensional ~2% cuts are always larger than those from the two-dimensional ~10% cuts (solid squares). This corroborates the statement that the variables N_{chgd} and KE_T do not autocorrelate with N_{IMF} in these data, as stricter cuts must magnify the importance of the conservation law that drives the autocorrelation.

The average multiplicities of IMFs are depicted versus the total charged particle multiplicity in Figure 3. For all of the available entrance channels and beam energies, the largest average multiplicities
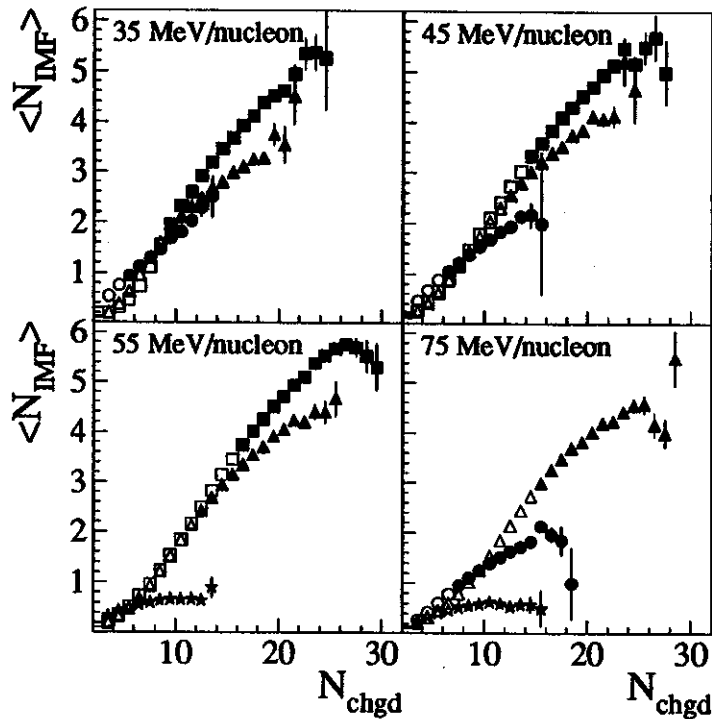

Figure 3: The average number of IMFs versus the total charged particle multiplicity for ^{20}Ne+^{27}Al (stars), ^{40}Ar+^{45}Sc (circles), ^{84}Kr+^{93}Nb (triangles), and ^{129}Xe+^{139}La (squares) reactions at four representative beam energies. The values for events above the ~10% most central thresholds on N_{chgd} are depicted as the solid points.

of IMFs are found in the events with the largest total charged particle multiplicities. In this Figure, the solid points for each system and beam energy are those above the ~10% cuts on N_{chgd} alone described above. A roughly universal dependence of $\langle N_{IMF} \rangle$ on N_{chgd} is noted for the more peripheral collisions (open points).

This analysis has investigated the average multiplicities of intermediate mass fragments emitted following central heavy-ion reactions in four near symmetric entrance channels, each at many intermediate beam energies. The average IMF multiplicities were shown to be significantly affected by possible autocorrelations with the variables upon which the impact parameter of each event was inferred. Six different centrality variables were compared, and those variables that are not autocorrelated with the IMF multiplicities for small impact parameter collisions were identified. These variables were the total charged particle multiplicity, N_{chgd}, and the total transverse kinetic energy, KE_T. Experimental observables other

49

than the IMF multiplicities were not studied in this paper, but general methods allowing the identification of autocorrelating centrality cuts for any experimental observable were described. The means and variances of N_{IMF} in events selected by one and two dimensional small impact parameter cuts on N_{chgd} and/or KE_T were presented versus the beam energy. The experimental values of $\langle N_{IMF} \rangle$ will be compared to the filtered predictions of a variety of models in the following article.

a. Hughes STX, Goddard Space Flight Center, Greenbelt, MD 20771
b. Department of Chemistry, SUNY - Stony Brook, Stony Brook, NY 11794
c. Department of Physics, U. of Michigan - Dearborn, Dearborn, MI 48128
d. Department of Physics and Astronomy, U. of Iowa, Iowa City, IA 52242
e. Cyclotron Institute, Texas A&M University, College Station, TX 77843

References

1. L.G. Moretto and G.J. Wozniak, Ann. Rev. Nucl. Part. Sci. (May, 1993).
2. A.S. Botvina, A.S. Iljinov, and I.N. Mishustin, Phys. Lett. B 205, 421 (1988);H.Y. Han *et al.*, Nucl. Phys. A492, 138 (1989); J. Hubele *et al.*, Phys. Rev. C 46, R1577 (1992).
3. R. Donangelo, J.A. López, and J. Randrup, Phys. Rev. C 48, 465 (1993).
4. G.D. Westfall *et al.*, Nucl. Inst. and Methods A238, 347 (1985).
5. G.D. Westfall *et al.*, Phys. Rev. Lett. 71, 1986 (1993); E. Bauge *et al.*, Phys. Rev. Lett. 70, 3705 (1993); T. Li *et al.*, Phys. Rev. Lett. 70, 1924 (1993); R.A. Lacey *et al.*, Phys. Rev. Lett. 70, 1224 (1993).
6. L. Phair *et al.*, Nucl. Phys. A548, 489 (1992).

INTERMEDIATE MASS FRAGMENT MULTIPLICITIES IN SMALL IMPACT PARAMETER HEAVY-ION COLLISIONS.

W.J. Llope, J.A. Conrad[a], C.M. Mader[b], G. Peilert[c], W. Bauer, D. Craig, E. Gualtieri,
S. Hannuschke, R.A. Lacey[d], J. Lauret[d], T. Li, A. Nadasen[e], E. Norbeck[f],
R. Pak, N.T.B. Stone, A.M. Vander Molen, G.D. Westfall, J. Yee, and S.J. Yennello[g].

In the previous article, methods for selecting small impact parameter heavy-ion reactions that do not autocorrelate with measurements of the multiplicities of intermediate mass fragments (IMFs) were described. The average IMF multiplicities in the central events so selected from a systematic set of experimental data were also presented. In this article, these average multiplicities will be compared to those obtained from events generated using a variety of models. The purpose of these calculations and comparisons is twofold. First, the different model were applied as consistently as possible, so that the average IMF multiplicities from the different models can be directly compared. Several investigations of this sort have been published [1], and these imply that larger average IMF multiplicities are obtained from multifragmentation models compared to consistently run sequential binary calculations. However, some disagreement with this claim was discussed in Ref. [2], following a study of calculated massive fragment ($Z \geq 5$) multiplicities. Second, under the assumption that the chosen input parameters to the different calculations are reasonably realistic, the average IMF multiplicities from the models can be directly compared to the experimentally measured values described in the previous article.

The event generation was performed in both dynamic and hybrid approaches. The "after-burners" used in the hybrid event generation were the Berlin [3] and Copenhagen [4] multifragmentation codes, as well as the sequential binary code Gemini [5]. The Berlin and Copenhagen codes are similar in philosophy, and assume that the system comes to thermal and chemical equilibrium within an expanded volume that is spherical and of prescribed radius. The various fragmentation channels occur with probabilities obtained from the channels' entropy, which is obtained using a finite temperature liquid drop model. The code Gemini pictures the disassembly as a sequence of binary fissions, using Bohr-Wheeler fission widths and conditional barriers from a shape adjusted two-spheroid finite range calculation, followed by evaporation according to a Hauser-Feshbach description.

All of these were run with the default parameters with the exception of the charge, mass, and excitation energy in the composite system, which was extracted from Boltzmann-Uehling-Uehlenbeck (BUU) calculations [6] in the same manner as described in Ref. [7]. These calculations describe the evolution of the one-body phase space distribution following the Boltzmann equation, including approximately Pauli-blocked scattering, via ensemble averaging. A soft equation of state was assumed, and the calculations were terminated when the radial density profile of the composite system most closely resembled that of a ground state nucleus [8]. The excitation energy of the excited system at rest in the center of momentum (CM) frame is then calculated as the total energy of this system minus a liquid-drop energy for a ground state nucleus with the same charge and mass. The calculations were performed at an impact parameter of $b = 0.20[R_P + R_T]$.

The excitation energies predicted by the BUU calculations for the selected events in each reaction are shown in Figure 1. A recent analysis [9] has noted differences in the IMF multiplicities obtained when an afterburner code is supplied with a single average excitation energy or excitation energies separately calculated for each event. However, given the large number of different reactions and afterburner model

codes studied here, a dynamic calculation of the afterburner input parameters for each generated event is computationally prohibitive. The mass and charge of the composite predicted by the BUU calculations is generally ~90% of the total entrance channel mass and charge. In the present BUU hybrid event generation, the remaining particles are thermally emitted from projectile and target-like sources, using reasonable assumptions for the velocities, temperatures, and emitted charge distributions of these sources for each reaction.
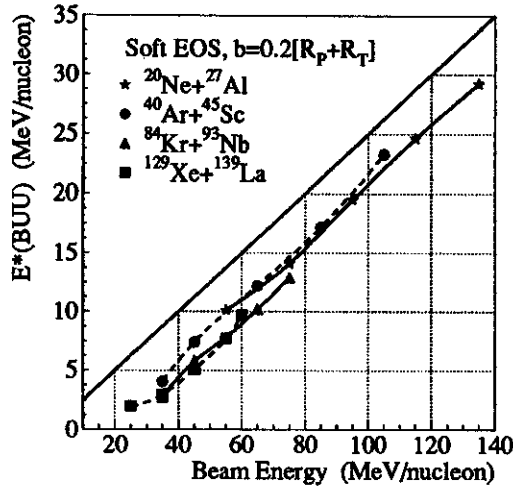

Figure 1: The excitation energies extracted from the BUU calculations for the ^{20}Ne+^{27}Al (stars), ^{40}Ar+^{45}Sc (circles), ^{84}Kr+^{93}Nb (triangles), and ^{129}Xe+^{139}La (squares) reactions, assuming an average impact parameter geometrically consistent with the present central event selection and a soft equation of state.

The Berlin and Gemini codes also require a cut-off angular momentum. For the BUU+Berlin calculations, the values used were $36\hbar$, $62\hbar$, $80\hbar$, and $70\hbar$ for the central ^{20}Ne+^{27}Al, ^{40}Ar+^{45}Sc, ^{84}Kr+^{93}Nb, and ^{129}Xe+^{139}La reactions, respectively. The angular momenta of the excited systems in the selected experimental events may very well exceed the values assumed above, presumably leading to decays involving a fast fission. The BUU+Gemini calculations were therefore also performed using cut-off angular momenta both well above and below the values listed above.

Complete events from a hybrid model involving a Quantum Molecular Dynamics (QMD) [10] initial stage and Copenhagen disassembly were also produced for ^{36}Ar+^{45}Sc reactions for impact parameters $b \leq 4$ fm. The QMD calculations describe the evolution of a system of gaussian wave packets (nucleons) that move under the influence of mutual two and three body forces and scatter in approximate respect of the Pauli principle. Although hybrid in the sense that the reaction is described in two steps, the QMD+Copenhagen calculations are dynamic in the sense that the impact parameter for each calculated event is known. Another model with this feature is the code Freesco [11], which does not require a separate BUU or QMD description of the initial stage of the reaction. This model divides the colliding nuclei into two spectator sources and a participant source, which share energy and angular momenta, according to the impact parameter. The decay of these sources is described by a microcanonical calculation similar in philosophy to those in the Berlin and Copenhagen models, including a simplified description of the evaporation.

A software reproduction of the experimental apparatus is used to filter the events obtained in all of the approaches listed above. This code contains a detailed treatment of the geometry of the device including all inactive regions, the run-dependent particle kinetic energy thresholds for all measurable particles, the

52

particle kinetic energy loss in the target and associated support assembly, and multiple particle hits in individual detector elements. The calculation of the result of a multiple hit involves the same particle charge and energy templates used to calibrate all of the raw experimental data. Following the passage through the filter code, the generated events appear as they would experimentally, up to a conservatively assumed systematic uncertainty of ~30% in the values of $\langle N_{IMF} \rangle$ from the filtered simulations.

The multiplicities of IMFs can also be calculated using model codes which do not generate samples of complete events. Examples of these are the statistical evaporation code of Ref. [12], and the Quantum Statistical Model [13]. The model of Ref. [12] follows the ensemble averaged evolution of a system that statistically emits particles in a sequence of two-body decay steps. This model thus provides a description of sequential binary disassembly that is alternative to the (fission-evaporation) Gemini code. The Fermi energy used as input in this model was 25 MeV for the central ^{20}Ne+^{27}Al and ^{40}Ar+^{45}Sc reactions, and 30 MeV for the central ^{84}Kr+^{93}Nb and ^{129}Xe+^{139}La reactions [14]. However, as complete events are not provided by this code, the experimental inefficiencies for the measurement of N_{IMF} can only be imposed approximately. This is done by extracting the average efficiency for detecting IMFs from each of the filtered event-generating models listed above for all entrance channels and beam energies. These efficiencies are generally between 50% and 80%, depending on the reaction and the approach used to generate the complete events. For each reaction separately, the minimum and maximum IMF measurement efficiencies obtained from the different model calculations are multiplied by the IMF multiplicities obtained from the statistical evaporation code. This defines a range of IMF multiplicities for each reaction presumed to contain the predictions of the statistical evaporation code including the effects of the experimental inefficiencies.

The average IMF multiplicities in the central ^{20}Ne+^{27}Al, ^{40}Ar+^{45}Sc, ^{84}Kr+^{93}Nb, and ^{129}Xe+^{139}La reactions are shown in Figure 2. The experimental values from the two-dimensional ~10% central cut (on N_{chgd} and KE_T) are shown by the solid points, while the values from the two one-dimensional ~10% cuts (on N_{chgd} and KE_T, separately) are given by the open points. The lines in the upper frames for each entrace channel are the values predicted by the filtered BUU+Berlin (solid), and BUU+Copenhagen (dashed) calculations. For the ^{40}Ar+^{45}Sc reactions only, the upper frame also includes the predictions of the filtered QMD+Copenhagen calculations, which were run under the same assumptions used to generate the BUU+Berlin and BUU+Copenhagen events. The lines in the middle frames for each entrance channel depict the predictions of the filtered Freesco code, which was run for maximum impact parameters of $0.01(R_P + R_T)$ (solid), $0.20(R_P + R_T)$ (dashed), and $0.40(R_P + R_T)$ (dot-dashed). The lower frames include the predictions of the filtered BUU+Gemini calculations, which were performed for maximum angular momenta of $10\hbar$ (solid), $70\hbar$ (dashed), and $200\hbar$ (dot-dashed).

The experimental IMF multiplicities in the central ^{20}Ne+^{27}Al reactions at beam energies near and above 100 MeV/nucleon agree with the BUU+Berlin, BUU+Copenhagen, and Freesco calculations. For lower beam energies in this system, however, the BUU+Berlin and BUU+Copenhagen calculations overestimate the experimental values. The calculated IMF multiplicities increase slowly with decreasing maximum impact parameters in the filtered Freesco calculations. The IMF multiplicities obtained from the filtered BUU+Gemini events increase with increases in the maximum angular momentum allowed in the calculation. However, even for maximum angular momenta well in excess of that which can be supported by the systems expected to be formed in the central ^{20}Ne+^{27}Al collisions, the BUU+Gemini IMF multiplicities underpredict the experimental values.

The filtered BUU+Berlin and BUU+Copenhagen calculations predict a sharp rise in the IMF multiplicities for the central ^{40}Ar+^{45}Sc reactions near beam energies of 40 MeV/nucleon. The experimental
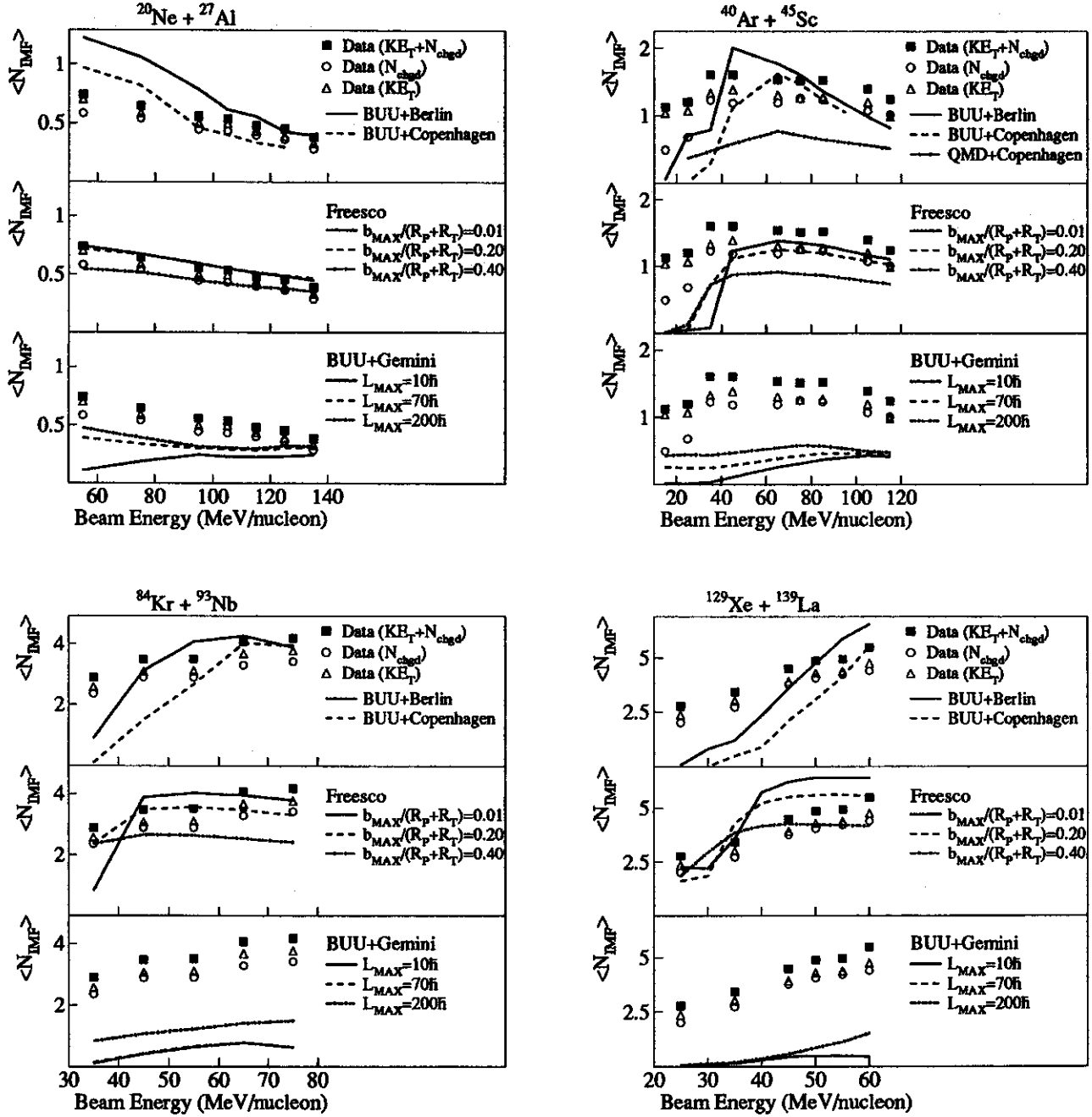
Figure 2: The average IMF multiplicities versus the beam energy in the central ^{20}Ne+^{27}Al, ^{40}Ar+^{45}Sc, ^{84}Kr+^{93}Nb, and ^{129}Xe+^{139}La reactions. The points are the experimental results for the events selected by the two-dimensional ~10% cuts on N_{chgd} and KE_T (solid squares), the one-dimensional ~10% N_{chgd} cuts (open circles), and by the one-dimensional ~10% KE_T cuts (open triangles). The lines depict the results from the various filtered model calculations (see text).

IMF multiplicities for these reactions exhibit such a rise for beam energies somewhere between 25 and 35 MeV/nucleon. These two approaches significantly underestimate the experimental IMF multiplicities below 35 MeV/nucleon, and reasonably reproduce the experimental values for larger beam energies. The ^{36}Ar+^{45}Sc QMD+Copenhagen calculations predict about a factor of two fewer IMFs on average than observed experimentally in the ^{40}Ar+^{45}Sc reactions for all beam energies. These QMD+Copenhagen predictions are quite insensitive to the maximum allowed impact parameter (from zero to 4 fm), the stiffness of the equation of state used in the QMD phase, or the radius of the critical freeze-out volume assumed in the subsequent Copenhagen calculation.

The filtered Freesco calculations predict a sharp rise in the IMF multiplicities near 35-45 MeV/nucleon, depending on the impact parameter region allowed in the calculation. These calculations generally reproduce the experimental results at beam energies above $\sim$45 MeV/nucleon if $b_{max} \lesssim 0.2(R_P + R_T)$, and again lead to significant underestimates at lower beam energies. The BUU+Gemini calculations significantly underestimate the experimental IMF multiplicities for all three values the maximum angular momenta allowed in these calculations and for all beam energies.

The conclusions drawn for the central ^{84}Kr+^{93}Nb and ^{129}Xe+^{139}La reactions are generally similar to those drawn from the central ^{40}Ar+^{45}Sc reactions. The BUU+Berlin and BUU+Copenhagen calculations underestimate the experimental IMF multiplicities at the lowest available beam energies, and provide a better reproduction of the experimental values at larger beam energies. The filtered Freesco calculations give a reasonable description on the IMF multiplicities for all of the available beam energies in these entrance channels. The BUU+Gemini calculations again lead to underestimates for all beam energies and maximum angular momenta allowed in the calculation.
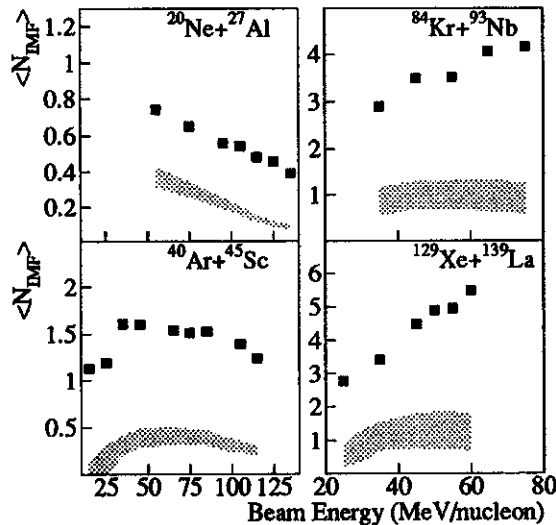

Figure 3: The average IMF multiplicities versus the beam energy experimentally measured using the two dimensional $\sim$10% central cuts (solid points), and calculated using the statistical evaporation model of Ref. [12] (shaded regions).

The comparison of the experimental IMF multiplicities and those from the statistical evaporation code of Ref. [12], following the approximate treatment of the experimental inefficiencies, is shown in Figure 3. For all of the reactions studied in this analysis, these calculations significantly underpredict the observed IMF multiplicities. This underprediction is similar to that from the filtered BUU+Gemini calculations.

In this article, predictions for the average multiplicities of IMFs in small impact parameter collisions were obtained from a variety of theoretical model codes. These predictions were filtered through a detailed software replica of the experimental apparatus. The average IMF multiplicities obtained from the various sequential binary models were always less than those obtained from the multifragmentation models. The experimental results were generally more accurately described by the multifragmentation models, with notable exceptions from some of these models for beam energies near and below ~35 MeV/nucleon.

a. Hughes STX, Goddard Space Flight Center, Greenbelt, MD 20771
b. Department of Physics, Hope College, Hope MI 49423
c. Lawrence Livermore National Laboratory, Livermore, CA 94550
d. Department of Chemistry, SUNY - Stony Brook, Stony Brook, NY 11794
e. Department of Physics, U. of Michigan - Dearborn, Dearborn, MI 48128
f. Department of Physics and Astronomy, U. of Iowa, Iowa City, IA 52242
g. Cyclotron Institute, Texas A&M University, College Station, TX 77843

References

1. A.S. Botvina, A.S. Iljinov, and I.N. Mishustin, Phys. Lett. B 205, 421 (1988);H.Y. Han *et al.*, Nucl. Phys. A492, 138 (1989); J. Hubele *et al.*, Phys. Rev. C 46, R1577 (1992).
2. R. Donangelo, J.A. López, and J. Randrup, Phys. Rev. C 48, 465 (1993).
3. D.H.E. Gross, Prog. Part. Nucl. Phys. 30, 155 (1993), and references therein.
4. J.P. Bondorf *et al.*, Nucl. Phys. A443, 321 (1985); J.P. Bondorf *et al.*, Nucl. Phys. A444, 460 (1985).
5. R.J. Charity *et al.*, Nucl. Phys. A483, 371 (1988).
6. W. Bauer *et al.*, Phys. Rev. C 34, 2127 (1986); W. Bauer, Phys. Rev. Lett. 61, 2534 (1988).
7. D.R. Bowman *et al.*, Phys. Rev. C 46, 1834 (1992).
8. C.M. Mader, Ph.D. Thesis, Michigan State University, 1993 (unpublished).
9. K. Kwiatkowski *et al.*, Phys. Rev. C 49, 1516 (1994).
10. J. Aichelin and H. Stöcker, Phys. Lett. B 176, 14 (1986); J. Aichelin *et al.*, Phys. Rev. C 37, 2451 (1988).
11. G. Fái and J. Randrup, Nucl. Phys. A404, 551 (1983).
12. W.A. Friedman and W.G. Lynch, Phys. Rev. C 28, 16 (1983).
13. H. Stöcker *et al.*, Nucl. Phys. A400, 63c (1983); D. Hahn and H. Stöcker, Nucl. Phys. A476, 718 (1988); D. Hahn and H. Stöcker, Phys. Rev. C 37, 1048 (1988).
14. W.A. Friedman, private communication.